International Journal of Earth Sciences (2021) 110:1453–1476
https://doi.org/10.1007/s00531-021-02024-w

ORIGINAL PAPER

Petrogenesis of a late-stage calc-alkaline granite in a giant S-type batholith: geochronology and Sr–Nd–Pb isotopes from the Nomatsaus granite (Donkerhoek batholith), Namibia

S. Aspiotis[1] · S. Jung[1] · F. Hauff[2] · R. L. Romer[3]

Received: 2 July 2020 / Accepted: 11 March 2021 / Published online: 7 April 2021

Abstract

The late-tectonic 511.4 ± 0.6 Ma-old Nomatsaus intrusion (Donkerhoek batholith, Damara orogen, Namibia) consists of moderately peraluminous, magnesian, calc-alkalic to calcic granites similar to I-type granites worldwide. Major and trace-element variations and LREE and HREE concentrations in evolved rocks imply that the fractionated mineral assemblage includes biotite, Fe–Ti oxides, zircon, plagioclase and monazite. Increasing K_2O abundance with increasing SiO_2 suggests accumulation of K-feldspar; compatible with a small positive Eu anomaly in the most evolved rocks. In comparison with experimental data, the Nomatsaus granite was likely generated from meta-igneous sources of possibly dacitic composition that melted under water-undersaturated conditions (X H_2O: 0.25–0.50) and at temperatures between 800 and 850 °C, compatible with the zircon and monazite saturation temperatures of 812 and 852 °C, respectively. The Nomatsaus granite has moderately radiogenic initial $^{87}Sr/^{86}Sr$ ratios (0.7067–0.7082), relatively radiogenic initial εNd values (− 2.9 to − 4.8) and moderately evolved Pb isotope ratios. Although initial Sr and Nd isotopic compositions of the granite do not vary with SiO_2 or MgO contents, $f^{Sm/Nd}$ and initial εNd values are negatively correlated indicating limited assimilation of crustal components during monazite-dominated fractional crystallization. The preferred petrogenetic model for the generation of the Nomatsaus granite involves a continent–continent collisional setting with stacking of crustal slices that in combination with high radioactive heat production rates heated the thickened crust, leading to the medium-P/high-T environment characteristic of the southern Central Zone of the Damara orogen. Such a setting promoted partial melting of metasedimentary sources during the initial stages of crustal heating, followed by the partial melting of meta-igneous rocks at mid-crustal levels at higher P–T conditions and relatively late in the orogenic evolution.

Keywords Nomatsaus granite · Donkerhoek batholith · Damara Orogen · Radiogenic isotopes · U–Pb monazite geochronology

Introduction

Granites carry information about (i) the melting conditions, (ii) the geochemical and isotopic character of the parental rocks, and (iii) the extent of fractional crystallization processes with or without assimilation (e.g. Castro 2013; Chappell et al. 2012; DePaolo 1981). It is generally agreed that partial melting of crustal lithologies (e.g. Chappell and White 2001; Collins et al. 1982), differentiation of primary, juvenile mantle-derived magmas (Frost and Frost 1997; Loiselle and Wones 1979; Turner et al. 1992), and interaction of juvenile material with older crustal rocks (Frost and Frost 1997) are the main processes that promote the generation and the geochemical evolution of granite melts.

✉ S. Aspiotis
stylianos.aspiotis@uni-hamburg.de

S. Jung
stefan.jung@uni-hamburg.de

F. Hauff
fhauff@geomar.de

R. L. Romer
rolf.romer@gfz-potsdam.de

[1] Mineralogisch-Petrographisches Institut, Universität Hamburg, Grindelallee 48, 20146 Hamburg, Germany

[2] GEOMAR Helmholtz-Zentrum für Ozeanforschung Kiel, Wischhofstrasse 1-3, 24148 Kiel, Germany

[3] Deutsches GeoForschungsZentrum GFZ, Telegrafenberg, 14473 Potsdam, Germany

Large-scale batholiths, i.e. the Sierra Nevada batholith that are generated above long-lived subduction zones are usually constructed over several tens of million years although the igneous activity occurred during several relatively brief pulses (i.e. Coleman and Glazner 1997; Wenner and Coleman 2004). In common subduction zone settings, the heat source is relatively well-known whereas in continent–continent collision scenarios where evidence for subduction zone magmatism is absent, the heat source for such protracted melting remains enigmatic. Alternative models include intrusion of hot mafic magmas into the crust (Bea 2012), advection of heat through long-lasting igneous activity (Patiño Douce et al. 1990; Bea 2012) and self-heating of the thickened continental crust through high contents of heat-producing elements (K, Th, U; England and Thompson 1986; Clark et al. 2011; Bea 2012). Especially the latter point may be important for the evolution of the Damara orogen as Haack et al. (1983) have shown that the crust of the Damara orogen is unusually rich in K, Th and U. In addition, Hall and Kisters (2016) and Kruger and Kisters (2016) have shown that pervasive meso-scale felsic magma migration through hot crust may provide also some extra heat for crustal melting.

For the Damara orogen, three major granitic suites are distinguished on basis of field relations and major and trace element as well as Nd, Sr, Pb and O isotope data, including (i) synorogenic granites formed by partial melting of metasedimentary rocks (Haack et al. 1982; McDermott et al. 1996; Paul et al. 2014), (ii) synorogenic granites, granodiorites and diorites derived from partial melting of older meta-igneous rocks from the underlying basement (e.g. Jung et al. 2002, 2003, 2015; McDermott et al. 1996; Ostendorf et al. 2014; Osterhus et al. 2014; Simon et al. 2017; Stammeier et al. 2015), and (iii) late-orogenic granites formed by partial melting of Pan-African igneous and/or metasedimentary sources (Jung et al. 1998; McDermott et al. 2000). The tectonic setting of the various Damaran igneous rocks, including the Donkerhoek batholith, was a matter of debate over the past 35 years. Tectonic models range from subduction-zone-related magmatism (Barnes and Sawyer 1980; Kasch 1983; Meneghini et al. 2014; Miller 2008) to intracrustal reworking and heat transfer in a continent–continent collision setting (Hartmann et al. 1983; Kröner 1982). Collectively, the majority of the ~ 560- to 500-Ma-old intrusive rocks of the Damara orogen, including the Donkerhoek batholith, represent crustal melts resembling common igneous rocks from continent–continent collisional settings.

In this study, we present new major and trace-element whole-rock data and U–Pb monazite isotope ages, as well as Nd, Sr and Pb isotope compositions from a part of the Donkerhoek batholith, the Nomatsaus granite. In addition, we discuss published O isotope data (Haack et al. 1982) in the context of the new data to constrain the possible sources involved in the generation of the granitic melts and to evaluate the influence of fractional crystallization and crustal assimilation processes. We show that the Nomatsaus granite is late-tectonic and has undergone only limited fractional crystallization.

Geological setting

The Neoproterozoic Damara orogen of Namibia is a deeply eroded and well-exposed part of the Pan-African mobile belt system in southern Africa. It is situated between the Congo Craton in the north, the Kalahari Craton in the south, and the Rio de la Plata Craton in the west (Miller 2008). The collision between the Congo craton and the Kalahari craton formed the NE–SW trending inland branch of the Damara belt (Fig. 1) (Miller 2008). The intracontinental branch of the Pan-African Damara belt can be subdivided into a Northern Zone (NZ), a Central Zone (CZ), and a Southern Zone (SZ), based on structure, stratigraphy, metamorphic grade, lithology, geochronology and aeromagnetic data (Miller 2008; Fig. 1).

The Northern Zone is characterized by peak metamorphic conditions of ~ 635 °C and ~ 0.87 GPa reflecting a typical HP/MT Barrovian metamorphism (Goscombe et al. 2017). The Central Zone represents a former magmatic arc and extends over an area of almost 75,000 km^2. It is dominated by intrusive rocks (96% granites and 4% diorites, tonalites, and granodiorites) that predominantly intruded between ~ 570 and ~ 480 Ma (Miller 2008). The igneous activity during that period is characterized by (i) ~ 570 Ma-old metaluminous amphibole-bearing granites derived from partial melting of meta-igneous sources (e.g. Bergemann et al. 2014), (ii) 560–540 Ma-old lower crust-derived diorites to granites (Jung et al. 2002, 2015; Milani et al. 2015; Ostendorf et al. 2014; Osterhus et al. 2014; Simon et al. 2017; Stammeier et al. 2015) that intruded coeval with voluminous ~ 550 Ma-old granodiorites and granites, and (iii) ~ 520–510 Ma-old granites derived from metapelitic sources (Paul et al. 2014). The metamorphic grade of the Central Zone increases from east to west with partial melting and granulite-facies conditions (Masberg et al. 1992). Peak conditions reached ~ 835 °C at ~ 0.5–0.6 GPa and occurred between ~ 520 and ~ 500 Ma (Jung et al. 2018; Longridge et al. 2017).

The boundary between the southernmost Central Zone and the Southern Zone is the Okahandja Lineament Zone (OLZ), which is thought to represent the suture of a Neoproterozoic intercontinental subduction of the Southern Zone beneath the Central Zone (Prave 1996). The OLZ marks the sharp transition of the high-T/low-P (~ 0.4–0.6 GPa) metamorphic rocks of the Central Zone to the high P/medium T metamorphic rocks (~ 0.8–0.9 GPa) of the Southern Zone.

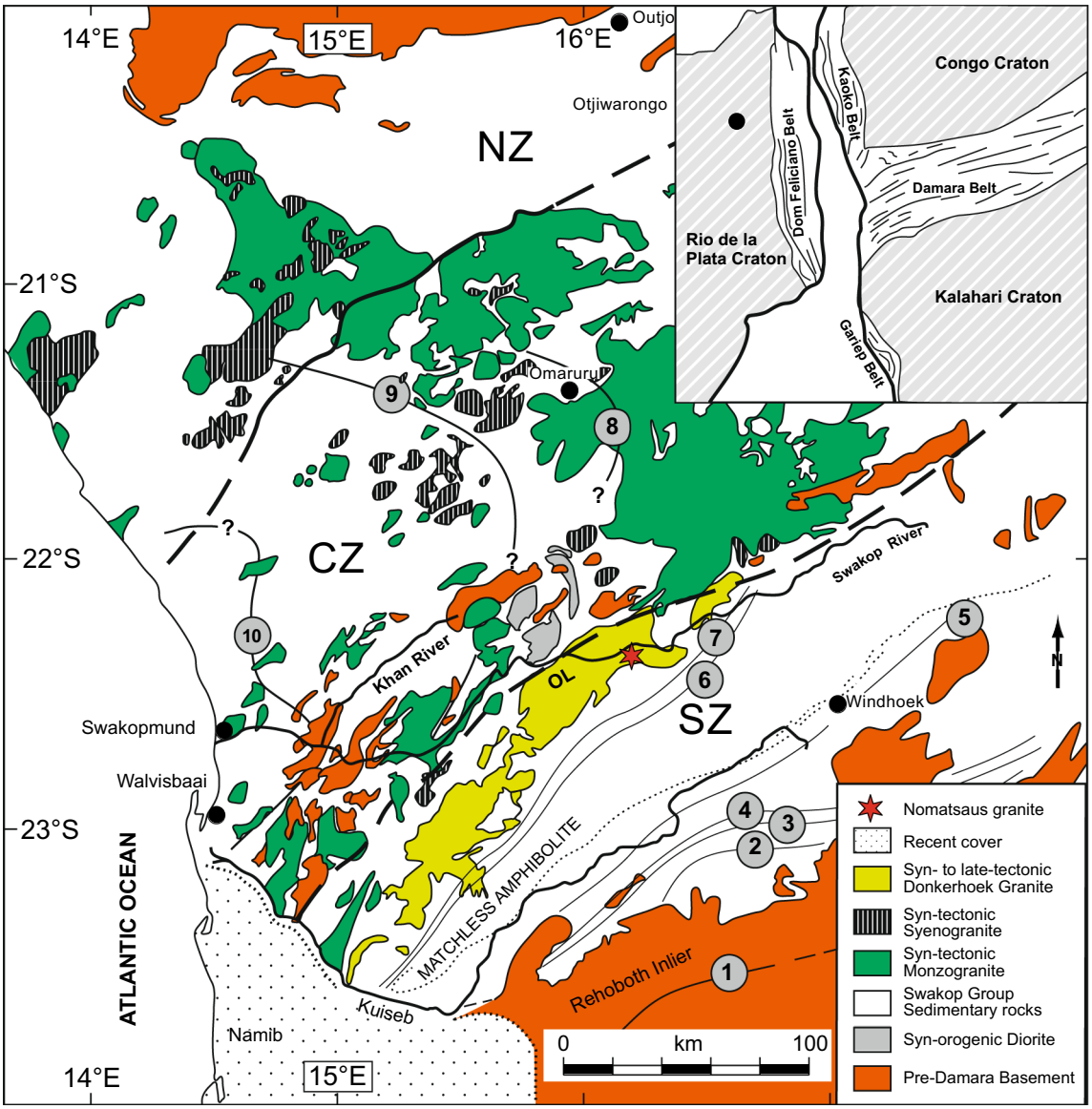

Fig. 1 Generalized geological map showing the study area within the Southern Zone of the Damara orogen, Namibia. *NZ* Northern Zone, *CZ* Central Zone, *SZ* Southern Zone. Distribution of the regional metamorphic isograds within the southern and central Damara orogen according to Hartmann et al. (1983). Isograds: (1) biotite-in; (2) garnet-in; (3) staurolite-in; (4) kyanite-in; (5) cordierite-in; (6) andalusite ↔ sillimanite; (7) sillimanite-in according to staurolite breakdown; (8) partial melting as a result of muscovite + plagioclase + quartz + H_2O ↔ melt + sillimanite; (9) K-feldspar + cordierite-in; (10) partial melting as a result of biotite + K-feldspar + plagioclase + quartz + cordierite ↔ melt + garnet. The star represents the approximate sampling locations near 22°20′S, 16°14′E

The Southern Zone represents the deeply eroded accretionary prism of the Damara Belt (Miller 2008) and dominantly consists of a thick (> 10 km) imbricated amphibolite-facies metaturbiditic sequence, the so-called Kuiseb Formation. Metamorphosed E-MORB mafic volcanic and plutonic rocks of the Matchless Amphibolite Belt form a > 350 km long belt of oceanic crust enfolded with the metaturbidites of the Kuiseb formation in the structurally lower parts of the prism (Meneghini et al. 2014). Barrovian-type metamorphism in the SZ shows a general increase from south to north, reaching maximum pressures of ~ 0.8–0.9 GPa and maximum temperatures of ~ 600–650 °C close to the OLZ between ~ 530 and ~ 517 Ma (Cross et al. 2015; Goscombe et al. 2017; Hartmann et al. 1983).

Along the low-pressure-sillimanite zone of the northern edge of the Southern Zone, the Donkerhoek batholith (Miller 2008) intruded with an estimated minimum volume of > 5000 km^3 (Fig. 1; Clemens et al. 2017). The main volume of the Donkerhoek granites was generated at pressures of ~ 0.6 GPa and > 800 °C, emplaced at ~ 0.45 GPa (Clemens

et al. 2017). The Donkerhoek batholith comprises mainly metaluminous to strongly peraluminous granites. Numerous late-tectonic dykes, pegmatites, and aplites occur also (Clemens et al. 2017; Miller 2008). The Donkerhoek batholith also includes minor volumes of magnesian, metaluminous to peraluminous calc-alkaline rocks, such as quartz diorites, monzogranites, granodiorite, and tonalite (Clemens et al. 2017; McDermott et al. 1996). The Kurikaub granodiorites and tonalites and the Nomatsaus granites are part of this suite. Based on recent U–Pb zircon and monazite dating (Clemens et al. 2017; Schwark et al. 2018 and references therein), the Donkerhoek batholith is distinguished into four groups, namely: (i) the ~ 541–535 Ma Onanis pluton; (ii) ~ 534 and ~ 526 Ma early granites and granodiorites, including the 527.5 ± 4.5 Ma-old Kurikaub granite; (iii) the ~ 532–510 Ma main Donkerhoek granite; and (iv) the ~ 514–505 Ma late-tectonic, crosscutting microgranitic dykes, aplites, and pegmatites. The age of the Nomatsaus intrusion is not well known. A Rb–Sr whole-rock isochron yields an age of 535 ± 8 Ma (recalculated from data of Blaxland et al. 1979 using the currently accepted decay constant for ^{87}Rb from Villa et al. 2015). Petrographic, mineralogical, and petrological information of the various rock types of the Donkerhoek granite are given in Table 1.

The Nomatsaus granite is located approximately at 22°20′S and 16°14′E (Fig. 1). Samples were taken from an area of ~ 4 × 5 km around this point. Exposures of the rock types are generally in the form of few isolated small-scale domes and flat-lying outcrops near river banks. Textures of the Nomatsaus granite are equigranular with generally no preferred orientation of the rock-forming minerals. Although outcrop evidence is restricted to small-scale domes at the river bank, the intrusion appears structureless. Enclaves are absent. The host rocks of the Nomatsaus intrusion are other granites of the Donkerhoek batholith, however, due to coverage of the area with gravel and sometimes grass beds contacts are not exposed.

The Nomatsaus granite is a true granite according to the classification of Middlemost (1994; Fig. 2). The main granite type is a holocrystalline medium to coarse-grained rock with subhedral to mainly anhedral granular textures. In some thin sections subpoikilitic grain shapes between feldspar and micas (mainly biotite and muscovite) are observed. Some samples demonstrate a faint foliation that is interpreted as a relic magmatic foliation with nearly parallel aligned mica sheets. The mineral assemblage of the granites is variable, consisting of quartz, K-feldspar, plagioclase, biotite, and sometimes muscovite. K-feldspar shows microcline twinning with partly perthitic exsolution. Plagioclase is not zoned and shows polysynthetic twinning. Quartz shows undulatory extinction and biotite typically appears as clusters that are commonly chloritized. Accessory minerals are zircon, apatite and monazite. Opaque minerals are mainly euhedral Fe–Ti oxides. Needle-shaped apatite and zircon are included in biotite, whereas chlorite may include rutile needles. Sericitization of K-feldspar and myrmekitic textures between plagioclase and quartz are common. Chlorite is a secondary mineral.

Geochronology

Six monazite fractions from sample S103 representing multigrain separates consisting of 3–5 grains were analyzed using U–Pb ID-TIMS. The analytical results are shown in Table 2. All samples have very radiogenic Pb isotopic composition, with measured ^{206}Pb/^{204}Pb ranging from ~ 2400 to ~ 106,000 (Table 2). Common lead was corrected using the Pb isotopic composition of leached K-feldspar (^{206}Pb/^{204}Pb = 18.37, ^{207}Pb/^{204}Pb = 15.69, ^{208}Pb/^{204}Pb = 38.16). Three monazite fractions fall on the concordia, whereas one fraction plot slightly above the concordia curve and one is strongly discordant (Fig. 3). Sample No. 1 differs from the other samples by having a considerably higher ^{232}Th/^{238}U and an older ^{207}Pb/^{206}Pb age (Table 2). As this fraction accounts for most of the scatter in the data, we omitted this fraction from the calculation of the discordia. The remaining five samples define a tightly constrained discordia that intercepts at 511.4 ± 0.6 Ma (2σ, MSWD = 0.59). Existing age determinations on samples of the Donkerhoek batholith including new U–Pb zircon and monazite dates indicate that the Donkerhoek batholith intruded between ~ 541 and ~ 508 Ma (Blaxland et al. 1979; Clemens et al. 2017; Schwark et al. 2018). The new age presented here places the intrusion of the Nomatsaus granite into the late stages of the emplacement of the batholith.

Geochemistry

Major and trace-element data

Major and trace-element compositions of the Nomatsaus granite are given in Table 3. The Nomatsaus granite is highly felsic (SiO_2 from 71.2 to 75.8 wt%) and slightly to strongly peraluminous with ASI (Alumina Saturation Index according to Frost et al. 2001) values ranging from 1.03 to 1.21 (Fig. 4). The samples are magnesian (with a Fe-index between 0.76 and 0.82; according to Frost et al. 2001) and most of them show a trend from calcic to calc-alkalic compositions with increasing SiO_2 concentrations (Fig. 4). Abundances of Na_2O, $FeO_{(total)}$, MgO, P_2O_5, CaO, Al_2O_3, and TiO_2 decrease with increasing SiO_2, whereas K_2O increase with increasing SiO_2 (Fig. 5).

Barium, Rb, Sr, and Zr are variable (341–876, 68–147, 161–290, 79–288 ppm, respectively, Table 3). Zirconium, Sr,

Table 1 Petrographic, mineralogical and petrological information for the various subunits of the Donkerhoek granite

Donkerhoek Batholith Groups	Rock type	Mineral assemblage	Age (Ma)	Rb/Sr	Rb/Ba	Na_2O (%)	CaO (%)	$^{87}Sr/^{86}Sr(i)$	εNd(i)	References
Onanis pluton	Granite	Kfs > Pl > Qtz > Bt ± Zrn ± Ti – Mt ± Ilm ± Ap ± Grt	~ 541–535	0.78–4.13	0.18–1.12	2.66–3.76	0.82–1.59	0.7099–0.7157	– 4.7 to – 12.3	Schwark et al. (2018)
Early granites, Granodiorites	Monzogranite, Granodiorite	Qtz – Kfs – Pl – Bt – Ms – Zrn – Ap – Mnz – Ilm	~ 534–526	0.31–0.93	0.16–0.34	2.28–3.14	2.17–4.40	0.7095	– 4.7	Clemens et al. (2017)
Kurikaub Granites	Diorite, Monzogranite	Pl – Qtz – Kfs – Ilm – Zrn – Ap – Aln – Ttn ± Bt ± Hbl ± Ms ± Sil	~ 528	0.11–0.36	0.06–0.17	2.81–4.05	1.07–6.47	0.7076	– 4.4	Clemens et al. (2017)
Main Donkerhoek Granites	Granites, rare Granodiorites, tonalites	Kfs > Pl > Qtz > Bt ± Grt ± Crd ± Sil ± Chl ± Ms ± Zrn ± Mnz ± Ap ± Ilm	~ 532–510	0.49–3.49	0.16–1.02	2.91–4.70	1.04–2.58	0.7083–0.7201	– 3.0 to – 12.9	Clemens et al. (2017)
	Monzogranite, Syenogranite			0.30–3.51	0.12–0.95	1.96–4.32	0.69–3.04	0.7052–0.7213	– 6.0 to – 13.8	Clemens et al. (2017)
Late microgranites	Granite	Pl – Kfs – Qtz – Ms – Bt ± Zrn ± Mnz ± Grt	~ 514–505	1.12–11.01	0.34–9.86	3.05–3.26	0.53–1.38	0.7101–0.7196	– 8.2 to – 11.9	Clemens et al. (2017)
Pegmatite, Aplite	Granite	Kfs > Qtz > Pl ± Bt ± Grt ± Ms ± Zrn ± Mnz	~ 531	3.40–39.6	1.21–8.04	2.93–4.38	0.25–0.74	0.7053–0.7097	– 3.7 to – 10.0	Jung and Hauff (2021)
Nomatsaus Granite	Granite	Pl > Qtz > Kfs > Bt > Ms ± Zrn ± Ap ± Chl ± Rt ± Ttn ± Ti – Mag ± Mnz	~ 511	0.29–0.76	0.08–0.27	2.63–4.48	1.0–2.04	0.7067–0.7082	– 2.9 to – 4.8	This study

Y, Ga, Th, U, and Pb abundances increase with decreasing SiO_2, whereas Rb and Ba show some scatter (Fig. 6). Rb/Sr ratios range from 0.29 to 0.76, Rb/Ba ratios vary from 0.08 to 0.27, and Sr/Ba ratios are between 0.19 and 0.72. The samples show enrichment of LREE over HREE (Fig. 7) with absolute REE concentrations ranging from 39 to 496 ppm (Table 3). $La/Yb_{(N)}$ ratios are variable ranging from 29.3 to 6.5, and $La/Sm_{(N)}$ and $Gd/Yb_{(N)}$ ratios range from 4.8 to 3.6 and 3.5 to 1.4, respectively. All samples (apart from S109: Eu/Eu* = 1.2) show substantial negative Eu anomalies (Eu/Eu* = 0.37–0.92) that become less prominent with increasing SiO_2 (Fig. 8).

Nd, Sr and Pb isotope data

The results of Nd, Sr and Pb isotope data are given in Table 4. Initial Nd and Sr isotopic ratios were calculated for 511 Ma. The initial εNd values are between − 2.9 and − 4.9 with initial $^{87}Sr/^{86}Sr$ ratios ranging from 0.7071 to 0.7082. Relative to granodiorites and granites from the adjacent southern Central Zone (Gawib pluton: Osterhus et al. 2014; Achas pluton: Simon et al. 2017; Bloedkoppie pluton: Stammeier et al. 2015), the samples of the Nomatsaus granite are characterized by relatively homogeneous Nd isotopic composition and moderately unradiogenic $^{87}Sr/^{86}Sr_{(i)}$ ratios (Fig. 9). Two-stage Nd model ages (Liew and McCulloch 1985) are in the range of 1.31–1.46 Ga. Lead isotope ratios from acid-leached feldspar separates reflect the initial values of the granites at the time of the last equilibration, based on the negligible amounts of U and Th in feldspar, and, thus, provide information about the crustal source rocks of the granites. The $^{206}Pb/^{204}Pb$, $^{207}Pb/^{204}Pb$, and $^{208}Pb/^{204}Pb$ ratios vary from 18.28 to 18.52, 15.67 to 15.71, and 38.03 to 38.38, respectively (Fig. 10). All samples plot close to the Pb evolution curve for the upper crust (Zartman and Doe 1981).

Discussion

The role of fractional crystallization and AFC processes

Figure 9 shows the initial $^{87}Sr/^{86}Sr$ and εNd isotopic composition of the Nomatsaus granite in comparison to other granites from the Donkerhoek batholith, lower crustal granodiorites and granites from the area (Gawib pluton: Osterhus et al. 2014; Achas pluton: Simon et al. 2017; Bloedkoppie pluton: Stammeier et al. 2015) and some basement gneisses. A conspicuous feature of the Nomatsaus granite is the relatively unradiogenic Sr and the relatively radiogenic Nd isotope composition, representing one of the least evolved granite suites of the Damara orogen. The narrow range of initial

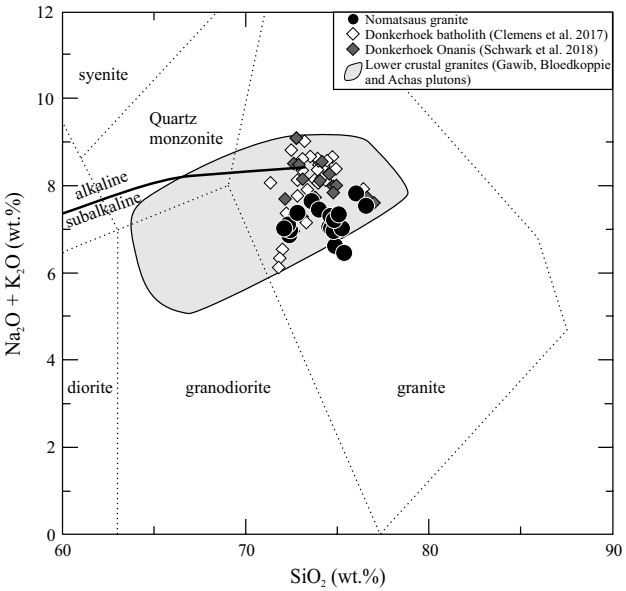

Fig. 2 Total alkali-silica (TAS) classification diagram of Middlemost (1994). Data from Table 3. Geochemical composition of other Donkerhoek batholith samples are taken from Schwark et al. (2018) and Clemens et al. (2017). Composition of lower crustal-derived granodiorites and granites (Bloedkoppie, Gawib and Achas plutons) are taken from Stammeier et al. (2015), Osterhus et al. (2014) and Simon et al. (2017)

$^{87}Sr/^{86}Sr$ and εNd values also indicates that (i) assimilation of evolved crust with radiogenic Sr isotopic composition was not important during the evolution of the granite (e.g. Schwark et al. 2018; Simon et al. 2017; Stammeier et al. 2015) and (ii) fractional crystallization was the dominant process.

The Nomatsaus granite displays decreasing Na_2O, $FeO_{(t.)}$, MgO, CaO, Al_2O_3, TiO_2, P_2O_5, Sr, Zr, Ga, U, Th, Sc, Y and V and increasing K_2O values with increasing SiO_2 contents (Figs. 5, 6) whereas Ba and Rb show some scatter (Fig. 6). The major element variation may reflect processes, such as sequential melting of one or more sources, restite unmixing or fractional crystallization. There is no field evidence for restite unmixing and the homogeneity in isotope composition argue against sequential melting of several sources. Sequential melting (with multiple melt extraction) of the same source at increasingly higher temperature is not in conflict with the small heterogeneity in the isotope composition (e.g. Wolf et al. 2019) but is incompatible with the REE variation where LREE and HREE decrease with increasing SiO_2. Moreover, progressive partial melting yielding peraluminous I-type granites will result in less peraluminous, even metaluminous compositions (Chappell et al. 2012) in the least evolved melts. This is not shown by the Nomatsaus granite with the least evolved melts being peraluminous. Therefore, these trends may indicate a common crystal fractionation process reflecting fractionation of

Table 2 U–Pb analytical data of monazite from the Nomatsaus intrusion, Donkerhoek batholith, Namibia

Sample[a]	Weight (mg)	Concentrations (ppm)		$^{206}Pb/^{204}Pb$	Isotope ratios (at%)[c]					Atomic ratios[c]			Apparent ages (Ma)[d]			Discord. – 1%[e]
		U	Pb_{tot}	Measured ratios[b]	$^{206}Pb/^{204}Pb$	$^{207}Pb/^{204}Pb$	$^{208}Pb/^{204}Pb$	$^{232}Th/^{238}U$	$^{206}Pb/^{238}U$	$^{207}Pb/^{235}U$	$^{207}Pb/^{206}Pb$	Rho	$^{206}Pb/^{238}U$	$^{207}Pb/^{235}U$	$^{207}Pb/^{206}Pb$	
Sample S 103																
Common lead $^{206}Pb/^{204}Pb = 18.37$, $^{207}Pb/^{204}Pb = 15.69$, $^{208}Pb/^{204}Pb = 38.16$																
1	0.018	2751	1262	2431	16.021	0.924	83.06	16.56	0.08445	0.6715	0.05767	0.9939	523	522	517	− 1.2
2	0.059	5809	1231	23,913	34.233	1.968	63.80	5.953	0.08381	0.6645	0.05750	0.9977	519	517	511	− 1.6
3	0.018	7739	1084	23,110	33.454	1.923	64.62	6.170	0.05414	0.4292	0.05749	0.9977	340	363	510	33
4	0.033	5904	1238	105,951	33.018	1.899	65.08	6.296	0.08008	0.6351	0.05752	0.9980	497	499	511	2.7
5	0.047	5938	1301	35,212	33.288	1.914	64.80	6.218	0.08439	0.6692	0.05751	0.9930	522	520	511	− 2.2
6	0.139	6261	1343	38,200	32.979	1.896	65.13	6.308	0.08183	0.6486	0.05749	0.9867	507	508	510	0.6

[a]Monazite concentrates were obtained using standard mineral-separation procedures and purified through separation by hand under the binocular. Monazite was dissolved using concentrated H_2SO_4 on the hot plate (160 °C) over night. To each sample, a ^{205}Pb-^{235}U mixed tracer was added before dissolution. U and Pb were separated using cation ion-exchange. Pb and U were loaded separately on single Re-filaments using colloidal silica and H_3PO_4 and measured at 1200–1260 °C and 1350–1400 °C, respectively, on a ThermoFisher Triton multicollector mass-spectrometer using Faraday collectors and ion counting

[b]Lead isotope ratios corrected for fractionation (0.1%/a.m.u.)

[c]Lead corrected for fractionation, blank, tracer contribution, and initial lead. During the measurement period total blanks were less than 15 pg for lead and less than 1 pg for uranium. $^{232}Th/^{238}U$ are calculated for an age of 510 Ma using the measured Pb isotopic compositions. Corrections for ^{206}Pb excess were insignificant, even for sample 1 that showed the largest correction as it had the highest $^{232}Th/^{238}U$ ($^{206}Pb/^{238}U_{corr} = 0.08440$ and $^{207}Pb/^{206}Pb_{corr} = 0.05771$)

[d]Apparent ages were calculated using $\lambda_{238} = 1.55125E{-}10\ year^{-1}$ and $\lambda_{235} = 9.848E{-}10\ year^{-1}$

[e]Per cent discordance calculated as $[1 - (^{206}Pb/^{238}U\ age)/(^{207}Pb/^{206}Pb\ age)] \times 100\%$

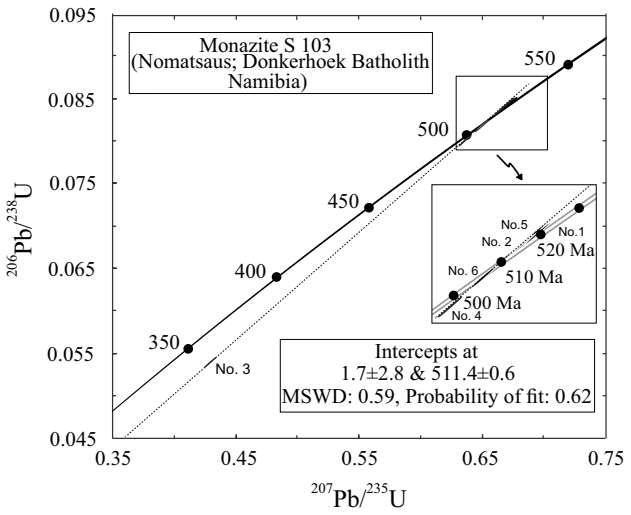

Fig. 3 U–Pb Concordia diagram showing U–Pb monazite analyses of the granite sample S103 of the Nomatsaus granite. Analysis no. 1 is not included in the calculation of the discordia

biotite ± muscovite, plagioclase, Fe–Ti oxides, zircon, monazite and possibly xenotime. Fractionation of two peraluminous mineral phases may have contributed to the decreasing ASI values with increasing SiO_2 and fractionation of monazite and xenotime may account for the general decrease in LREE and HREE together with a decrease in P_2O_5 with increasing SiO_2. The weak positive correlation between Eu and Sr suggests some fractionation of plagioclase. Although K-feldspar has, similar to plagioclase, a large positive Eu anomaly (Bea et al. 1994), the variation in the size of the Eu anomaly cannot be related to fractionation of K-feldspar because K_2O increases with increasing SiO_2. As the most fractionated sample displays a weak positive Eu anomaly, there may have been minor accumulation of K-feldspar during the final stages of fractional crystallization.

Among the Nomatsaus granite samples, depletion of LREE and HREE (Fig. 7) correlates with differentiation, as the most evolved samples have the lowest LREE and HREE abundances. Decreasing LREE and HREE abundances are accompanied by the development of a weak positive Eu anomaly with increasing SiO_2 and decreasing Eu contents (Fig. 8). Two of the least evolved samples are enriched in LREE and HREE suggesting some accumulation/retention of REE-enriched accessory phases (monazite and xenotime). For the other samples, depletion in LREE and HREE with increasing fractional crystallization indicates that fractional crystallization removed significant amounts of accessory phases, such as monazite (LREE) and xenotime (HREE). Note that, sample S109 has particularly high SiO_2 concentrations among the studied granites. As high SiO_2 contents in melt increase apatite solubility and delay apatite saturation to later magmatic stages (Harrison and Watson 1984), earlier crystallizing accessory REE phases (monazite, xenotime) incorporate most of the LREE.

To quantify this process, we have applied a simple Rayleigh fractionation model (Fig. 11). Using the composition of sample S 104, which is one of the least fractionated samples, as starting composition, the fractionation of 30% biotite, 10% K-feldspar, and 60% plagioclase at $f = 0.6$ (f = fraction of melt remaining) yielded an evolved melt with slightly reduced LREE abundances, a prominent negative Eu anomaly and virtually unchanged HREE abundances. This composition does not agree well with the measured composition of the Nomatsaus granite samples. Removing in addition 0.38% monazite and 0.22% xenotime during fractionation, however, strongly decreased LREE and HREE abundances and produced a small positive Eu anomaly as observed for sample S 109. Because xenotime/liquid partition coefficients for REE are not available, we have calculated apparent partition coefficients for xenotime/liquid by combining monazite/liquid (Stepanov et al. 2012) and monazite/xenotime (Andrehs and Heinrich 1998) partition coefficients.

The result of this simple modelling is also supported by the negative trend in the $f^{Sm/Nd}$ vs $\varepsilon Nd_{(i)}$ plot (Fig. 12, e.g. Jung et al. 2011). The Nomatsaus granite plots in the quadrant that is characterized by LREE enrichment (negative $f^{Sm/Nd}$, where $f^{Sm/Nd}$ is the enrichment factor of Sm relative to Nd in a sample relative to CHUR; Shirey and Hanson 1986) and negative initial εNd values and follow a trend towards less negative $f^{Sm/Nd}$ and less radiogenic initial εNd values. Less negative $f^{Sm/Nd}$ values indicate a "flattening" of the LREE pattern which can only be explained by removal of a mineral, such as monazite, that strongly prefers LREE over MREE and HREE (for a more detailed study see Jung et al. 2011). Fractionation of apatite cannot account for the trend seen in Fig. 12, as apatite typically is depleted in LREE relative to MREE (Watson and Green, 1981).

Possible sources of the Nomatsaus granite and constraints on partial melting processes

Previous studies have shown that felsic magnesian calc-alkaline granitic magmas are mainly generated by AFC processes operating on basaltic parental magmas (Bacon and Druitt 1988) or by partial melting of mafic to intermediate igneous sources (Chappell and Stephens 1988; for a recent review see Gao et al. 2016).

The magnesian medium- to high-K slightly peraluminous calc-alkaline Nomatsaus granite is enriched in Ba (341–876 ppm) and Sr (160–290 ppm) relative to Rb (68–147 ppm), which in combination with high Na_2O (mostly > 2.6 wt%) and moderate CaO (mainly 1.0–2.0 wt%) contents is indicative of granites from non-pelitic sources. For comparison, granites derived from pelitic sources usually have $Na_2O < 3.5$ wt%, $CaO < 1.2$ wt%, 70–100 ppm Sr

Table 3 Major (in wt.%) and trace element (in ppm) compositions of the Nomatsaus granite

	S100	S101	S 103	S104	S105	S 106	S108	S109	S110	S111	S112
SiO_2	74.22	71.56	74.14	72.20	71.76	74.73	73.42	75.83	74.11	73.32	74.77
TiO_2	0.24	0.33	0.29	0.33	0.28	0.28	0.20	0.15	0.28	0.22	0.25
Al_2O_3	13.73	14.79	13.58	15.23	15.22	13.32	14.81	12.95	13.34	14.63	13.46
Fe_2O_3	1.94	2.57	2.11	2.51	2.27	1.89	1.56	1.07	1.95	1.67	1.76
MnO	0.03	0.03	0.03	0.08	0.06	0.02	0.03	0.02	0.02	0.02	0.03
MgO	0.45	0.63	0.54	0.60	0.47	0.51	0.33	0.27	0.53	0.39	0.47
CaO	1.53	2.04	1.66	2.01	2.03	1.52	1.39	1.19	1.61	1.59	1.49
Na_2O	3.68	4.48	4.06	4.17	4.43	3.48	3.75	3.08	3.52	3.79	3.38
K_2O	3.23	2.32	2.50	2.87	2.62	3.85	3.66	4.40	2.84	3.82	3.62
P_2O_5	0.05	0.09	0.09	0.14	0.13	0.08	0.10	0.10	0.09	0.10	0.09
LOI	0.97	0.59	0.51	0.44	0.53	0.63	0.64	0.80	0.43	0.25	0.48
Sum	100.07	99.43	99.51	101.00	99.80	100.31	99.89	99.86	98.72	99.80	99.80
ASI	1.12	1.18	1.16	1.18	1.18	1.13	1.16	1.02	1.16	1.10	1.09
Li	32.3	n.d.	37.1	n.d.	n.d.	n.d.	n.d.	23.3	35.7	n.d.	36.8
Sc	2.20	5	2.77	7	4	4	3	1.01	2.35	5	2.48
V	16.4	32	23.1	35	22	22	11	10.8	21.9	19	18.0
Cr	11.2	12	6.50	14	12	10	6	7.79	7.53	8	9.31
Co	2.03	n.d.	2.73	n.d.	n.d.	n.d.	n.d.	1.28	2.70	n.d.	2.34
Ni	1.53	3	1.78	3	3	2	2	1.54	1.66	3	1.59
Zn	28.0	25	27.7	24	21	21	16	11.8	22.9	11	21.2
Ga	18.8	26	20.9	27	23	17	16	15.2	19.9	20	18.0
Rb	67.5	107	98.0	114	100	73	147	131	71.0	114	92.0
Sr	230	234	228	257	270	244	239	231	161	236	191
Y	13.2	24	17.2	53	38	22	14	7.05	25.0	16	8.63
Zr	174	199	211	288	272	176	104	78.5	135	126	117
Nb	7.31	11	10.3	9	10	11	7	5.61	10.9	9	9.88
Ba	773	448	368	545	598	341	840	833	462	607	586
Hf	4.32	n.d.	5.13	n.d.	n.d.	n.d.	n.d.	2.04	3.46	n.d.	3.01
Ta	0.489	n.d.	0.579	n.d.	n.d.	n.d.	n.d.	0.318	0.593	n.d.	0.547
Pb	20.7	25	16.0	29	31	16	30	21.3	16.6	29	19.7
Th	11.2	19	15.1	35	29	13	4	3.01	8.49	9	5.22
U	1.39	5	3.99	6	6	5	2	3.64	1.95	2	1.34
La	26.8	60.0	42.6	121	100	n.d	24.0	8.51	23.2	30.0	14.8
Ce	47.0	106	84.1	203	172	n.d	41.0	15.4	44.8	54.0	28.3
Pr	5.80	n.d.	9.48	n.d.	n.d.	n.d.	n.d.	1.89	5.36	n.d.	3.33
Nd	21.3	44.0	35.2	91.0	79	n.d.	17.0	7.05	20.2	23.0	12.4
Sm	3.85	8.1	6.39	18.0	14.7	n.d.	3.76	1.38	4.06	4.30	2.40
Eu	0.859	1.1	0.989	1.9	1.6	n.d.	0.84	0.515	0.738	1.00	0.663
Gd	3.14	6.5	5.15	13.1	10.6	n.d.	2.99	1.24	3.81	3.99	2.01
Tb	0.433	n.d.	0.692	n.d.	n.d.	n.d.	n.d.	0.190	0.628	n.d.	0.293
Dy	2.35	5.05	3.58	9.78	6.78	n.d.	2.61	1.16	4.07	3.52	1.61
Ho	0.457	n.d.	0.627	n.d.	n.d.	n.d.	n.d.	0.234	0.847	n.d.	0.307
Er	1.28	2.15	1.65	4.95	2.90	n.d.	1.05	0.676	2.44	2.00	0.842
Tm	0.187	n.d.	0.234	n.d.	n.d.	n.d.	n.d.	0.103	0.370	n.d.	0.127
Yb	1.24	1.90	1.53	4.00	2.60	n.d.	1.15	0.681	2.40	1.70	0.854
Lu	0.191	0.30	0.230	0.55	0.38	n.d.	0.18	0.102	0.337	0.23	0.128
$T_{Zr(sat.)}$ (°C)	806	812	822	850	843	802	765	738	786	775	771
$T_{mnz(sat.)}$ (°C)	782	852	828	922	904	n.d.	770	696	776	792	739

	S116	S117	S118	S119	S 1111	S1112	S1113
SiO_2	72.95	71.83	71.46	74.06	73.63	75.48	73.78

Table 3 (continued)

	S116	S117	S118	S119	S 1111	S1112	S1113
TiO_2	0.20	0.29	0.31	0.21	0.20	0.14	0.25
Al_2O_3	14.31	14.67	15.02	14.19	13.93	13.12	14.31
Fe_2O_3	1.62	2.09	2.18	1.41	1.67	1.32	1.80
MnO	0.04	0.03	0.04	0.03	0.02	0.04	0.04
MgO	0.35	0.52	0.62	0.34	0.40	0.30	0.36
CaO	1.30	1.81	2.03	1.52	1.56	1.00	1.35
Na_2O	3.63	4.25	4.45	3.83	3.62	2.63	4.00
K_2O	3.24	3.03	2.49	3.35	3.60	5.13	3.00
P_2O_5	0.08	0.11	0.14	0.12	0.08	0.12	0.08
LOI	0.49	0.60	0.41	0.33	0.74	0.67	0.69
Sum	98.21	99.23	99.15	99.39	99.45	99.95	99.66
ASI	1.21	1.13	1.18	1.13	1.09	1.01	1.19
Li	n.d.	n.d.	n.d.	n.d.	22.0	n.d.	n.d.
Sc	3	3	3	3	2.23	3	4
V	14	23	26	15	13.4	7	16
Cr	8	11	8	7	6.20	5	8
Co	n.d.	n.d.	n.d.	n.d.	1.74	n.d.	n.d.
Ni	3	2	2	3	1.18	2	3
Zn	17	26	30	15	17.3	19	23
Ga	23	21	23	20	18.7	20	17
Rb	123	105	97	96	71.8	130	100
Sr	228	274	283	273	168	171	290
Y	15	14	15	16	12.2	18	25
Zr	103	151	156	198	134	82	161
Nb	7	7	8	8	6.31	5	4
Ba	720	640	492	717	869	510	876
Hf	n.d.	n.d.	n.d.	n.d.	3.58	n.d.	n.d.
Ta	n.d.	n.d.	n.d.	n.d.	0.573	n.d.	n.d.
Pb	28	27	27	27	20.1	23	30
Th	9	9	6	11	8.93	4	17
U	2	3	4	4	1.87	1	3
La	25.0	37.0	38.0	30.0	24.4	22.0	50.0
Ce	46.0	63.0	64.0	51.0	45.0	38.0	89.0
Pr	n.d.	n.d.	n.d.	n.d.	5.41	n.d.	n.d.
Nd	20.0	28.0	30.0	23.0	20.2	17.0	36.0
Sm	4.20	4.88	5.49	4.55	3.77	3.76	6.86
Eu	0.74	0.90	0.95	0.83	0.856	0.75	1.04
Gd	3.62	4.01	4.00	2.99	3.06	3.42	5.85
Tb	n.d.	n.d.	n.d.	n.d.	0.424	n.d.	n.d.
Dy	2.73	2.62	2.78	2.47	2.27	3.69	3.83
Ho	n.d.	n.d.	n.d.	n.d.	0.426	n.d.	n.d.
Er	1.20	1.20	1.20	1.15	1.16	1.80	1.75
Tm	n.d.	n.d.	n.d.	n.d.	0.170	n.d.	n.d.
Yb	1.15	0.85	1.00	0.85	1.11	1.65	1.80
Lu	0.18	0.15	0.15	0.14	0.173	0.24	0.26
$T_{Zr(sat.)}$ (°C)	768	788	791	818	781	745	803
$T_{mnz(sat.)}$ (°C)	779	807	810	790	777	765	836

Zircon and monazite saturation temperatures according to Watson and Harrison (1983) and Montel (1993), respectively

LOI loss on ignition, *n.d.* not determined, *ASI* Alumina saturation index $Al_2O_3/(CaO - 3.3P_2O_5 + Na_2O + K_2O)$

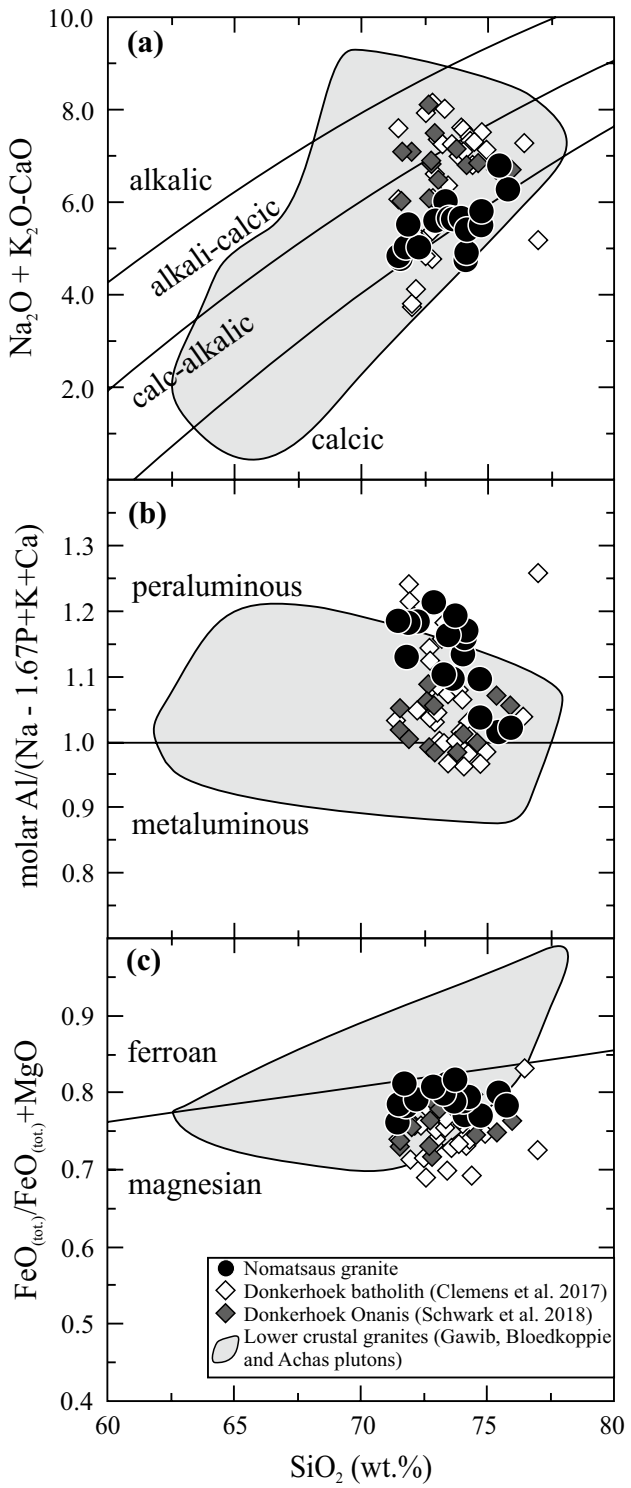

Fig. 4 Alumina saturation values (ASI), MALI values (MALI = $Na_2O + K_2O$–CaO; modified alkali lime index; Frost et al. 2001) and Fe-index plotted against SiO_2 concentrations for the Nomatsaus granite. Data from Table 3. Geochemical composition of lower crustal-derived granodiorites and granites [Bloedkoppie, Gawib and Achas plutons from Stammeier et al. (2015), Osterhus et al. (2014) and Simon et al. (2017), respectively] as in Fig. 2

and 220–260 ppm Ba, Miller 1985). These features together with the low Rb/Sr (0.29–0.76) and Rb/Ba (0.08–0.27) ratios indicate that the Nomatsaus granite has affinities to granites derived from meta-igneous sources (Rb/Sr: 0.11–0.19 and Rb/Ba: 0.09–0.16; e.g. Simon et al. 2017), rather than metapelitic sources (Rb/Sr: ~4 and Rb/Ba: ~1; e.g. Paul et al. 2014). The Nomatsaus samples are less peraluminous than typical granites from pelitic sources (Fig. 13) and, thus, require a feldspar-rich source (Moyen et al. 2017). Thus, possible sources are restricted to meta-igneous rocks and feldspar-rich, mica-poor metagreywackes. Kuiseb-type metasedimentary rocks of the Southern Zone (Schwark et al. 2018) have far more radiogenic Sr and less radiogenic Nd isotopic compositions than the Nomatsaus granite (Fig. 9) and, therefore, cannot represent a source. Typical Damaran mafic meta-igneous rocks, i.e., the Matchless amphibolites, will yield felsic melts with radiogenic εNd values (εNd at 511 Ma: ca. +8; Hawkesworth et al. 1981; Fig. 9). Re-melting of pre-tectonic granodiorites and granites can be ruled out because these rock types have mostly unradiogenic initial εNd and radiogenic initial $^{87}Sr/^{86}Sr$ values ($\varepsilon Nd_{(511)}$ between − 5.1 and − 14.3, $^{87}Sr/^{86}Sr_{(511)}$: 0.711–0.717; McDermott et al. 1996; Fig. 9).

Meta-igneous sources producing granitic melts by partial melting mainly fall into the following three groups: (i) Felsic orthogneisses with a granodioritic composition that melted at moderately high temperatures of 700–800 °C and low pressures of 0.3–0.5 GPa at water-saturated to water-undersaturated conditions (Holtz and Johannes 1991). Melting at these conditions usually leads to strongly peraluminous leucogranites poor in Ti, Mg, Ca, and Na, which is very common in migmatites. (ii) Amphibolites to metatonalites commonly yield granitic melts in the temperature range 900–1000 °C (Patiño Douce and Beard 1995). Medium- to high-K calc-alkaline granites are produced at temperatures of 875–1000 °C over a wide range of pressures between 0.3 and 1.5 GPa (Patiño Douce and Beard 1995). In addition, partial melting of amphibole- and biotite-bearing metavolcanoclastic rocks at temperatures between 850 and 1050 °C and pressures of 1.0 and 2.0 GPa (Skjerlie and Johnston 1996) yields strongly peraluminous, calcic, ferroan, and high-K melts, which in comparison to the Nomatsaus granite are too poor in Na_2O, but enriched in Al_2O_3. Fluid-present melting of low-K metabasaltic sources (Beard and Lofgren 1991) can be excluded as this process produces low-K, ferroan, strongly peraluminous melts rich in Ca and Al and poor in Mg. (iii) Dacitic sources may produce granites at moderate to high temperatures of 675–950 °C at pressures of 1.0 GPa and water-saturated to water-undersaturated conditions (Conrad et al. 1988). Partial melting of dacitic sources at temperatures of 800–850 °C and X H_2O between 0.25 and 0.50 (Conrad et al. 1988) produces melts that show the same major element composition as the least evolved samples

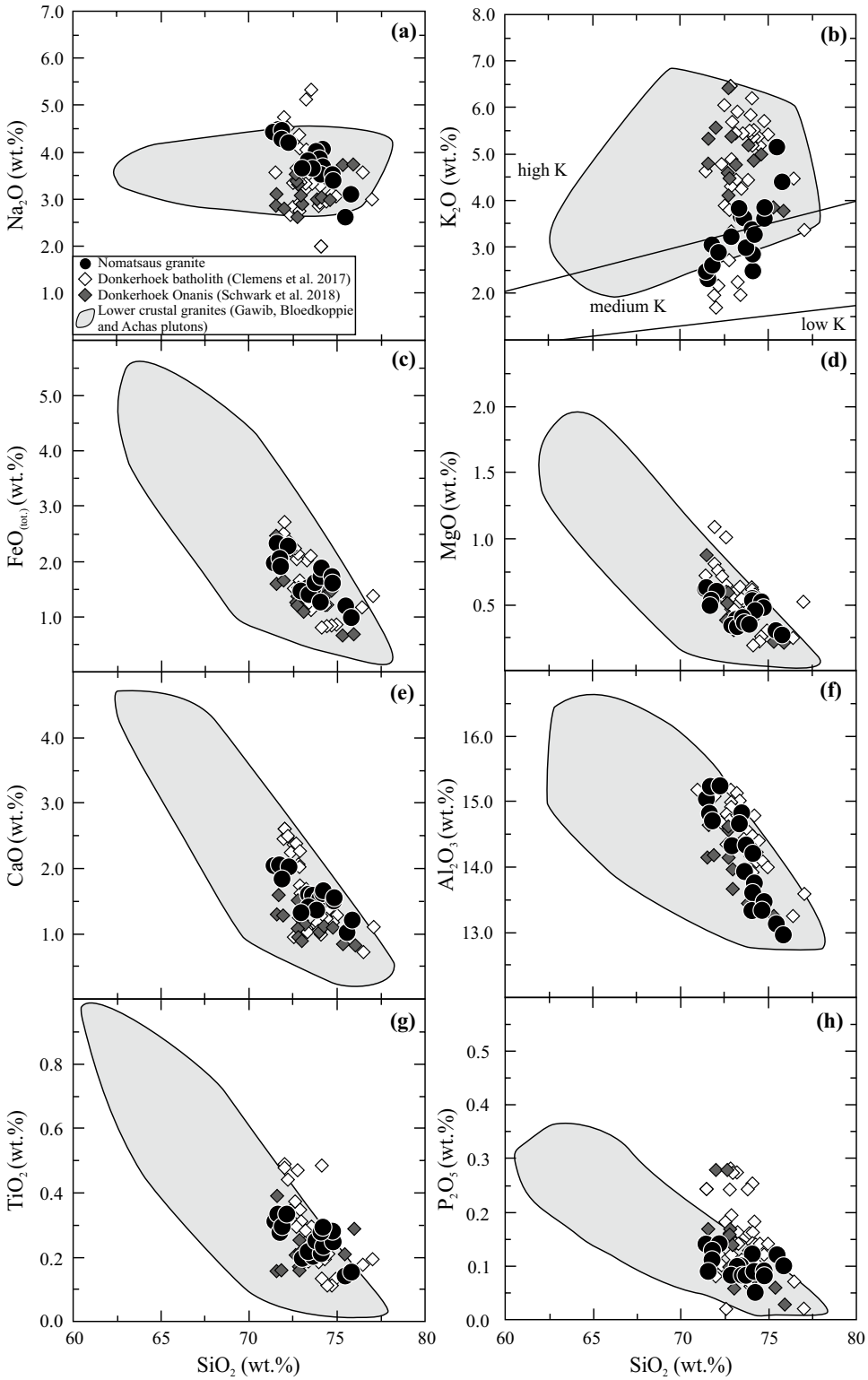

Fig. 5 Selected major elements plotted against SiO_2 concentrations for the Nomatsaus granite. Data from Table 3. Geochemical composition of lower crustal-derived granodiorites and granites [Bloedkoppie, Gawib and Achas plutons from Stammeier et al. (2015), Osterhus et al. (2014) and Simon et al. (2017), respectively] as in Fig. 2

from the Nomatsaus granite. These considerations agree with those of Clemens et al. (2011), who emphasized that volcanic arc rocks of intermediate composition, like dacites and andesites, are the likely source rocks for metaluminous to fairly peraluminous granite melts.

Note that in the study of Conrad et al. (1988), partial melting of greywackes yielded partial melts very similar to those derived from dacite melting (Fig. 14). The reason for this is that the greywacke composition used by Conrad et al. (1988) contains large amounts of detrital volcanogenic

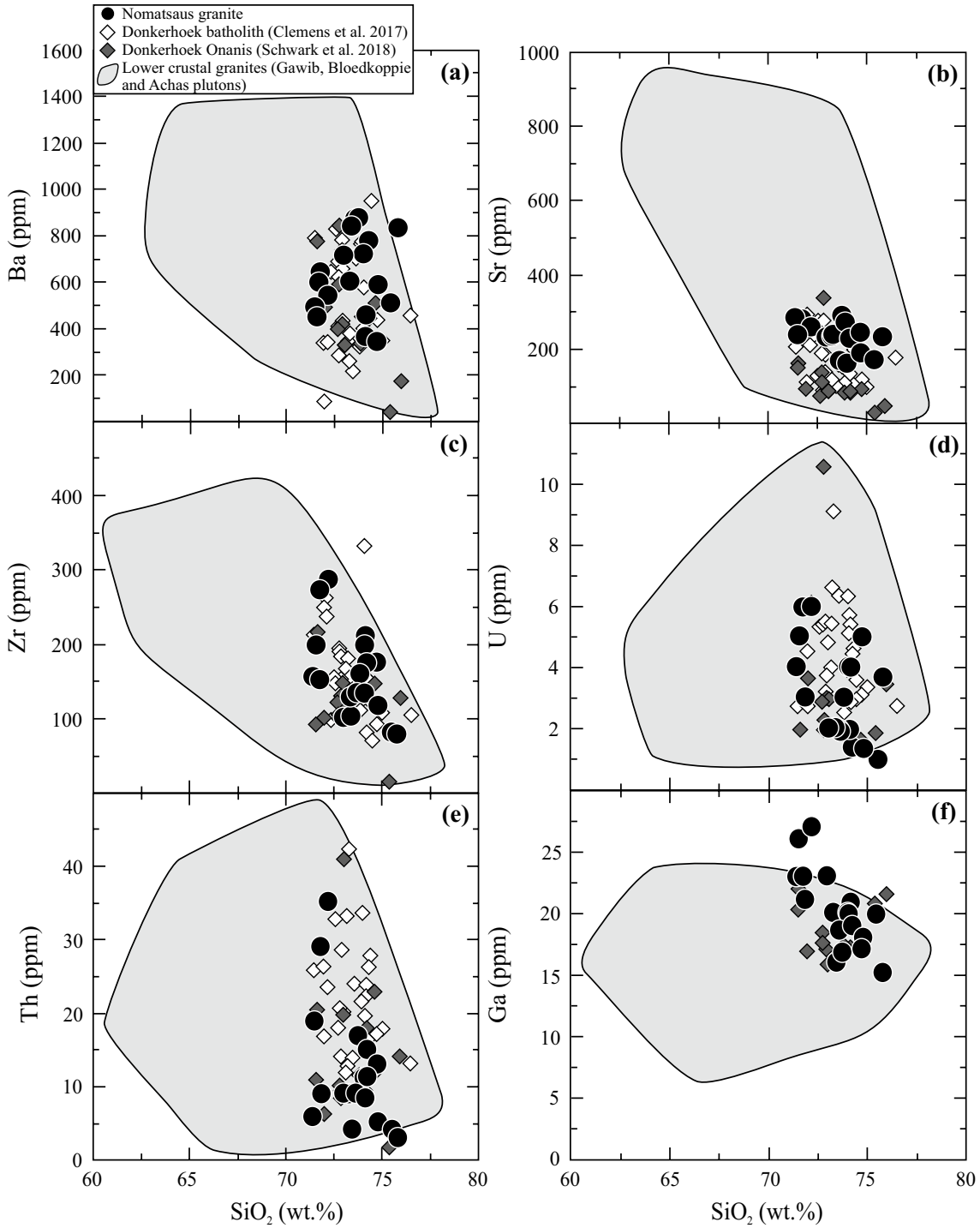

Fig. 6 Selected trace-element diagrams for the Nomatsaus granite. Geochemical composition of lower crustal-derived granodiorites and granites [Bloedkoppie, Gawib and Achas plutons from Stammeier et al. (2015), Osterhus et al. (2014) and Simon et al. (2017), respectively] as in Fig. 2

material. For the Nomatsaus granites, a similar metasedimentary source is unlikely because the oxygen isotope composition of the Nomatsaus granite (~ 10‰; Haack et al. 1982) does not match the high $\delta^{18}O$ values of typical Damaran metasedimentary rocks ($\delta^{18}O$: 12–15‰; Haack et al. 1982). However, it cannot be ruled out that greywackes similar to those used by Conrad et al. (1988) are present at depth.

Pressure and temperature conditions of partial melting can be estimated using the least evolved granitic samples, inferring that those samples represent the chemical

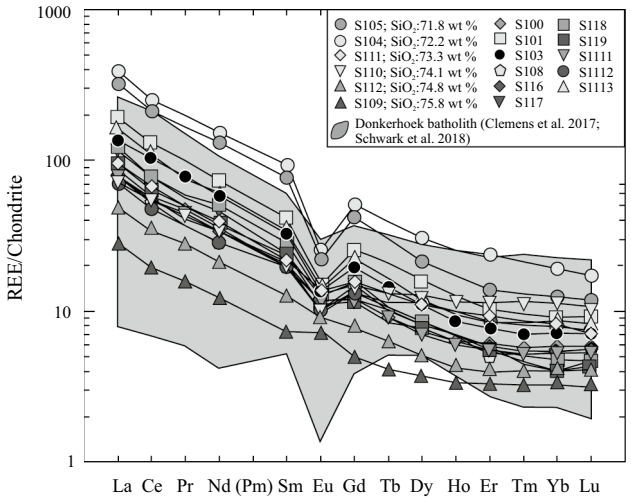

Fig. 7 Chondrite-normalized Rare-Earth Element (REE) showing the composition of distinct granite samples of the Nomatsaus granite. Chondrite normalization values after Boynton (1984)

composition of near-primary melts. Light rare-earth element abundances indicate that two samples (S 104 and S 105; Table 2) are enriched in LREE suggesting some accumulation of monazite. The other samples show decreasing LREE contents with increasing SiO_2 and using the least evolved sample from this suite (sample S 101), zircon saturation (Watson and Harrison 1983) and monazite saturation (Montel 1993) temperatures are 812 and 852 °C, respectively (Table 3). Few studies have shown that monazite can contain a residual component (Copeland et al. 1988; Rapp and Watson 1986; Sawka et al. 1986) whereas other studies suggested that monazite is rarely residual at the temperatures of anatexis in the lower crust (> 850 °C; Rapp et al. 1987, Yakymchuk and Brown 2014). The geochronological data obtained in this study show that monazite is not residual implying that the mineral saturation results are reliable estimates. The calculated saturation temperatures are in good agreement with the experimental data of Conrad et al. (1988) indicating temperatures of 800–850 °C at X H_2O values of 0.25–0.50, respectively. Moreover, a temperature of 850 °C allows biotite dehydration melting, which is the main process generating granitic melts that are able to leave the source (e.g., Le Breton and Thompson 1988; Vielzeuf and Holloway 1988). Pressure estimates for the formation and emplacement of the Nomatsaus granite based on experimental work in the Qz–Ab–Or system (Fig. 15; Anderson and Bender 1989; Long et al. 1986), indicate that the primitive Nomatsaus granite was generated at pressures between 0.4 and 0.5 GPa under water-undersaturated conditions of 5 wt% H_2O. The most evolved samples may suggest emplacement conditions at pressures of c. 0.2 GPa. These results are compatible with those from Clemens et al. (2017) who suggested 0.4–0.5 GPa at c. 850 °C for the generation of most Donkerhoek granites.

General implications

Implications on the sources

There is evidence that granites with different geochemical signatures indicating distinct sources can occur within the same batholith (i.e. Hu et al. 2019; Merino Martínez et al. 2014) and that large-scale plutons grow incrementally from various sources (i.e., Glazner et al. 2004). Numerous studies have shown that peraluminous granites can be generated through melting of metasedimentary sources, remelting of

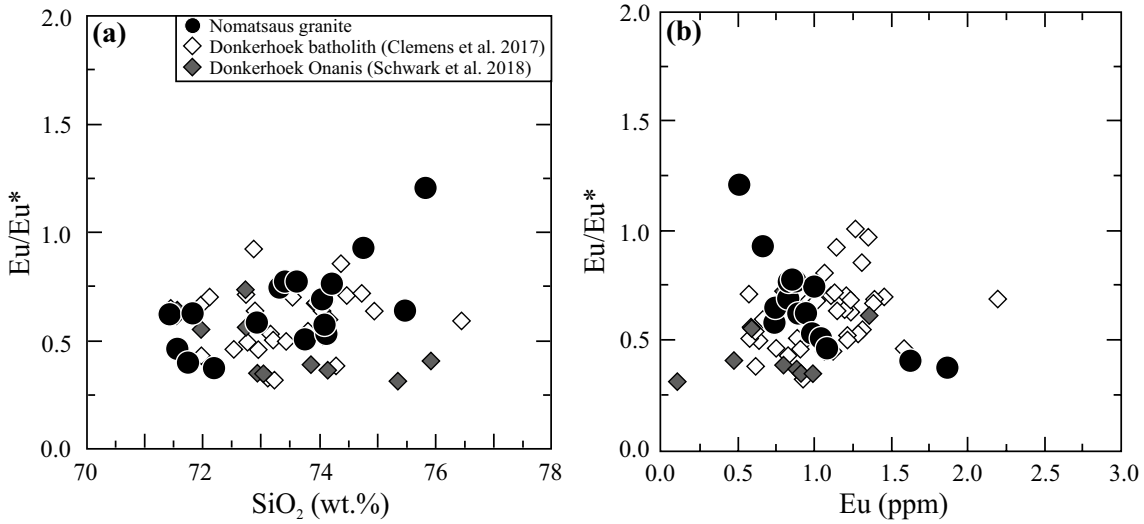

Fig. 8 Plots of Eu/Eu* ratios (Eu* = Eu/$\sqrt{}$Sm*Gd) vs. **a** SiO_2 abundances and **b** Eu (ppm) concentrations from the Nomatsaus granite

Table 4 Sr and Nd whole rock isotope data and Pb isotope ratios obtained on acid-leached K-feldspar from the Nomatsaus granite

	S100	S101	S 103	S104	S105	S 106	S108	S109	S110
$^{87}Rb/^{86}Sr$	0.85	1.32	1.24	1.28	1.07	0.87	1.78	1.64	1.28
$^{87}Sr/^{86}Sr_{(m)}$	0.713370	0.716857	0.717059	0.716431	0.714898	0.714470	0.720208	0.719770	0.717459
2SE	0.000005	0.000005	0.000005	0.000006	0.000004	0.000005	0.000007	0.000007	0.000005
$^{87}Sr/^{86}Sr_{(i)}$	0.707179	0.707221	0.708001	0.707083	0.707093	0.708165	0.707247	0.707820	0.708153
$^{147}Sm/^{144}Nd$	0.109	0.111	0.110	0.119	0.113	0.112	0.134	0.118	0.122
$^{143}Nd/^{144}Nd_{(m)}$	0.512132	0.512155	0.512145	0.512146	0.512147	0.512144	0.512178	0.512178	0.512191
2SE	0.000004	0.000004	0.000003	0.000005	0.000004	0.000004	0.000005	0.000004	0.000005
$^{143}Nd/^{144}Nd_{(i)}$	0.511767	0.511784	0.511778	0.511746	0.511770	0.511769	0.511731	0.511783	0.511784
$\varepsilon Nd_{(i)}$	− 4.2	− 3.8	− 3.9	− 4.6	− 4.1	− 4.1	− 4.9	− 3.8	− 3.8
T-1_{DM} (Ga)	1.32	1.31	1.31	1.44	1.35	1.34	1.61	1.37	1.40
T-2_{DM} (Ga)	1.41	1.38	1.39	1.44	1.40	1.41	1.46	1.39	1.38
$f^{Sm/Nd}$	− 0.45	− 0.44	− 0.44	− 0.39	− 0.43	− 0.43	− 0.32	− 0.40	− 0.38
$^{206}Pb/^{204}Pb$	18.43	n.d.	18.37	n.d.	18.37	18.34	n.d.	18.32	18.28
$^{207}Pb/^{204}Pb$	15.69	n.d.	15.69	n.d.	15.70	15.70	n.d.	15.68	15.68
$^{208}Pb/^{204}Pb$	38.35	n.d.	38.16	n.d.	38.15	38.20	n.d.	38.06	38.06
	S111	S112	S116	S117	S118	S119	S 1111	S1112	S1113
$^{87}Rb/^{86}Sr$	1.40	1.39	1.56	1.11	0.99	1.02	1.24	2.20	1.00
$^{87}Sr/^{86}Sr_{(m)}$	0.717549	0.718274	0.719181	0.715352	0.714528	0.715202	0.716011	0.723665	0.715065
2SE	0.000006	0.000006	0.000006	0.000005	0.000006	0.000004	0.000005	0.000006	0.000005
$^{87}Sr/^{86}Sr_{(i)}$	0.707369	0.708146	0.707813	0.707277	0.707305	0.707792	0.707011	0.707644	0.707799
$^{147}Sm/^{144}Nd$	0.113	0.117	0.127	0.105	0.111	0.120	0.113	0.134	0.115
$^{143}Nd/^{144}Nd_{(m)}$	0.512183	0.512168	0.512165	0.512184	0.512198	0.512193	0.512162	0.512229	0.512167
2SE	0.000004	0.000004	0.000004	0.000005	0.000004	0.000004	0.000003	0.000004	0.000004
$^{143}Nd/^{144}Nd_{(i)}$	0.511805	0.511778	0.511740	0.511832	0.511828	0.511793	0.511785	0.511782	0.511782
$\varepsilon Nd_{(i)}$	− 3.4	− 3.9	− 4.7	− 2.9	− 3.0	− 3.7	− 3.8	− 3.9	− 3.9
T-1_{DM} (Ga)	1.30	1.37	1.52	1.21	1.25	1.37	1.33	1.52	1.35
T-2_{DM} (Ga)	1.35	1.39	1.45	1.31	1.32	1.37	1.38	1.39	1.39
$f^{Sm/Nd}$	− 0.43	− 0.41	− 0.35	− 0.46	− 0.44	− 0.39	− 0.43	− 0.32	− 0.41
$^{206}Pb/^{204}Pb$	n.d.	18.29	18.45	18.33	n.d.	18.33	18.47	18.41	n.d.
$^{207}Pb/^{204}Pb$	n.d.	15.67	15.70	15.67	n.d.	15.68	15.70	15.71	n.d.
$^{208}Pb/^{204}Pb$	n.d.	38.03	38.30	38.04	n.d.	38.06	38.17	38.17	n.d.

$^{87}Rb/^{86}Sr$ and $^{147}Sm/^{144}Nd$ are calculated from ICP-MS data from Table 2. Calculation of εNd values is relative to CHUR according to Jacobsen and Wasserburg (1980). Single-stage Nd model ages (T-1_{DM}) calculation is according to Michard et al. (1985) and second-stage Nd Model ages (T-2DM) are calculated according to Liew and McCulloch (1985)

(m.) measured, *(i.)* initial

andesitic to rhyolitic sources (Chappell et al. 2012; Gao et al. 2016), through fractional crystallization of I-type granites (Chappell 1999; Miller 1985) or entrainment of peritectic or non-peritectic mineral assemblages (Chappell et al. 2012; Clemens et al. 2011). In addition, Clemens (2018) pointed out that mildly peraluminous I-type granites with variable radiogenic Sr and unradiogenic Nd isotope compositions may not be generated from meta-igneous sources, but represent melts from sedimentary sources. These sources must be quite distinct to the common Al-rich metasedimentary sources that yield common S-type granites.

The magnesian and calc-alkaline Nomatsaus granite with higher Na_2O, CaO and Sr contents than common S-type granites features the main characteristics of I-type granites. Among the granites of the Damara orogen, the Nomatsaus granite is distinctive by its fairly unradiogenic Sr and radiogenic Nd isotopic compositions and its rather light oxygen isotopic composition (Haack et al. 1982), which contrasts with the heavy oxygen isotopic composition of typical S-type granites from the Damara orogen (Jung et al. 1999). The Donkerhoek batholith in general has been interpreted as a S-type granite (Clemens et al. 2017), though subsequent work implies that I-type granites are also present (Schwark et al. 2018). These studies have shown that the Sr–Nd isotopic composition of the S-type granites from the Donkerhoek batholith is more heterogeneous than those

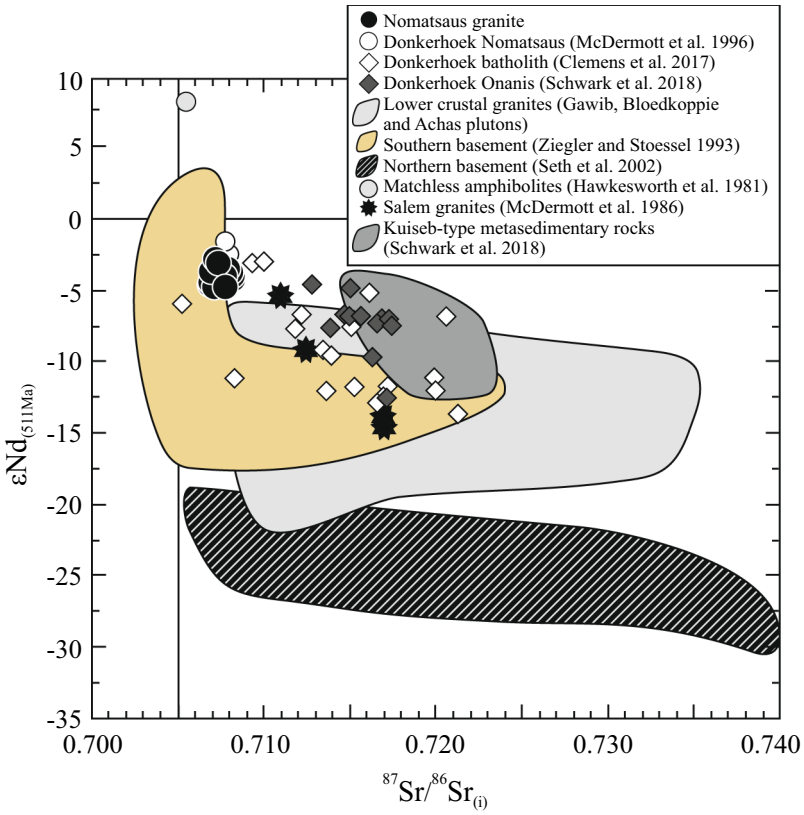

Fig. 9 Initial εNd vs. initial $^{87}Sr/^{86}Sr$ diagram for the Nomatsaus granite. Geochemical composition of lower crustal-derived granodiorites and granites [Bloedkoppie, Gawib and Achas plutons from Stammeier et al. (2015), Osterhus et al. (2014) and Simon et al. (2017), respectively] as in Fig. 2. Composition of the Kalahari craton (Southern Basement) according to Ziegler and Stoessel (1993) and composition of the Congo craton basement (Northern Basement) is taken from Seth et al. (2002)

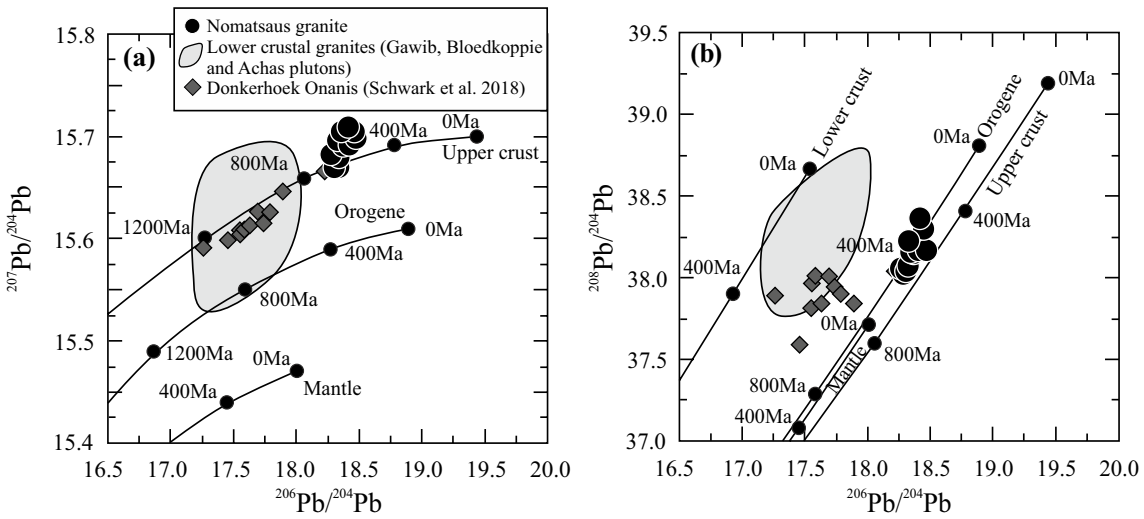

Fig. 10 Plots of **a** $^{207}Pb/^{204}Pb$ and **b** $^{208}Pb/^{204}Pb$ vs. $^{206}Pb/^{204}Pb$ isotope ratios of leached feldspar from the Nomatsaus granite. Geochemical composition of lower crustal-derived granodiorites and granites (Bloedkoppie, Gawib and Achas plutons from Stammeier et al. (2015), Osterhus et al. (2014) and Simon et al. (2017), respectively) as in Fig. 2. Pb growth curves according to Zartman and Doe (1981). Tick marks represent 400 Ma intervals

of metasedimentary rocks from the Southern Zone of the orogen. A significant number of samples from the Donkerhoek batholith shows less radiogenic Sr but similar Nd isotopic compositions than the metasedimentary rocks from the Southern Zone which must result from the involvement of unknown sources. Data from the Onanis I-type granites (Schwark et al. 2018) show only marginal overlap with the metasedimentary rocks from the Southern Zone and the Nomatsaus granite show no overlap at all (Fig. 9). Similarly, oxygen isotopes of the metasedimentary rocks (12.9–14.7‰;

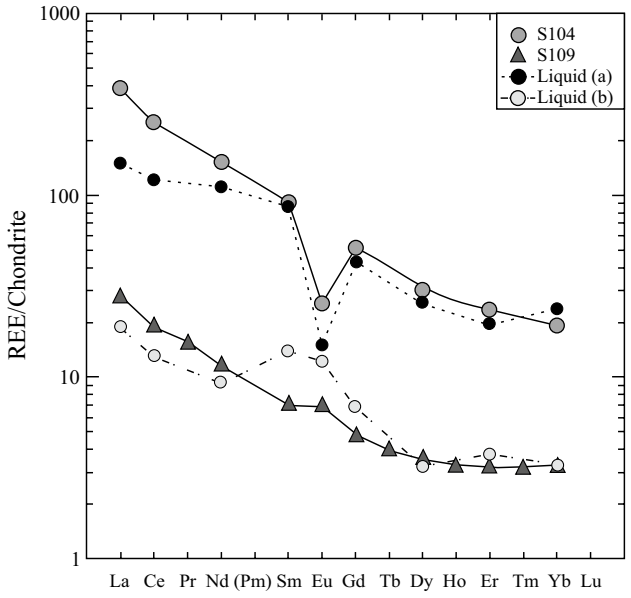

Fig. 11 Chondrite-normalized REE plot showing the results of fractional crystallization modelling including the effects of monazite and zircon fractionation on the composition of a granitic liquid. Sample S 104 represents the source composition and Sample S 109 shows the most fractionated sample of the Nomatsaus pluton. The dashed line (liquid a) represents the composition of the granite melt after fractional crystallization of 30% biotite, 10% K-feldspar and 60% plagioclase and the dash-dotted line (liquid b) represents the composition of the liquid after additional removal of 0.38% monazite and 0.22% xenotime. Mineral partition coefficients for biotite, plagioclase, K-feldspar, monazite, and zircon are from Bea et al. (1994). Chondrite values are from Boynton (1984)

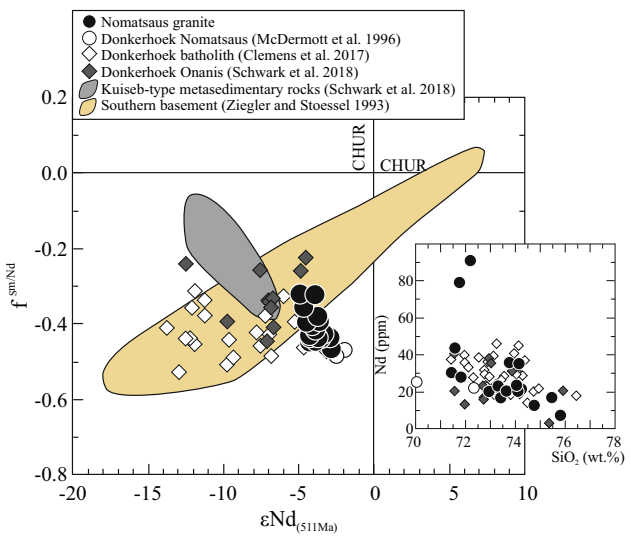

Fig. 12 $f^{Sm/Nd}$ vs. εNd plot for the Nomatsaus granite and reference fields for basement rocks of the Proterozoic Rehoboth Inlier, metasedimentary rocks from the Kuiseb Formation, and the Donkerhoek batholith. The role of monazite fractionation is shown in the inset. For further discussion, see text

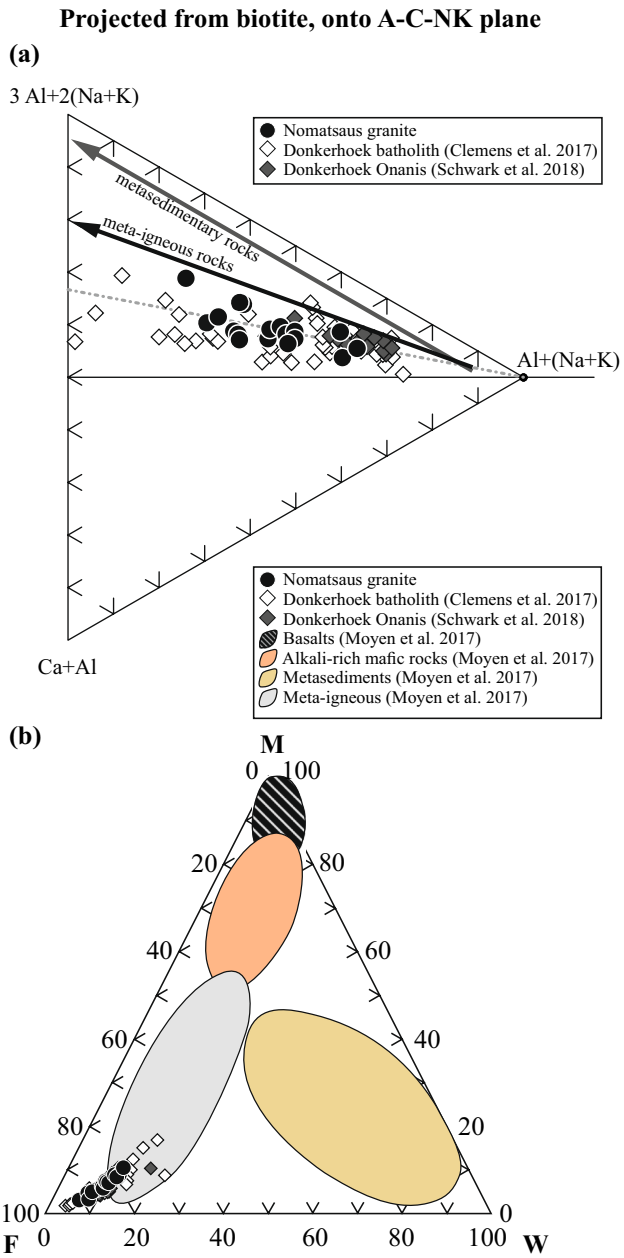

Fig. 13 Triangular diagrams of the granites of the Nomatsaus area (**a**) projected from biotite onto the Ca + Al—3Al + 2(Na + K)—Al + (Na + K) plane (Moyen et al. 2017). The dotted line indicates the evolution of the Nomatsaus granites, which requires a source richer in feldspar than average granites derived from typical metasedimentary and meta-igneous rocks (arrows). **b** Triangular MFW projection of Ohta and Arai (2007). M corresponds to mafic rocks, F to felsic rocks and W to weathered compositions. Also shown are compositions of experimental liquids from basaltic, alkali-rich mafic, metasedimentary and meta-igneous sources (Moyen et al. 2017)

Haack et al. 1982; 11.6–13.6‰; Jung et al. 2000) overlap with those obtained from S-type granites (13.8–15.2‰; Jung et al. 1999) but are significantly heavier than those for the Nomatsaus granite (9.4–10.7‰; Haack et al. 1982). The Pb

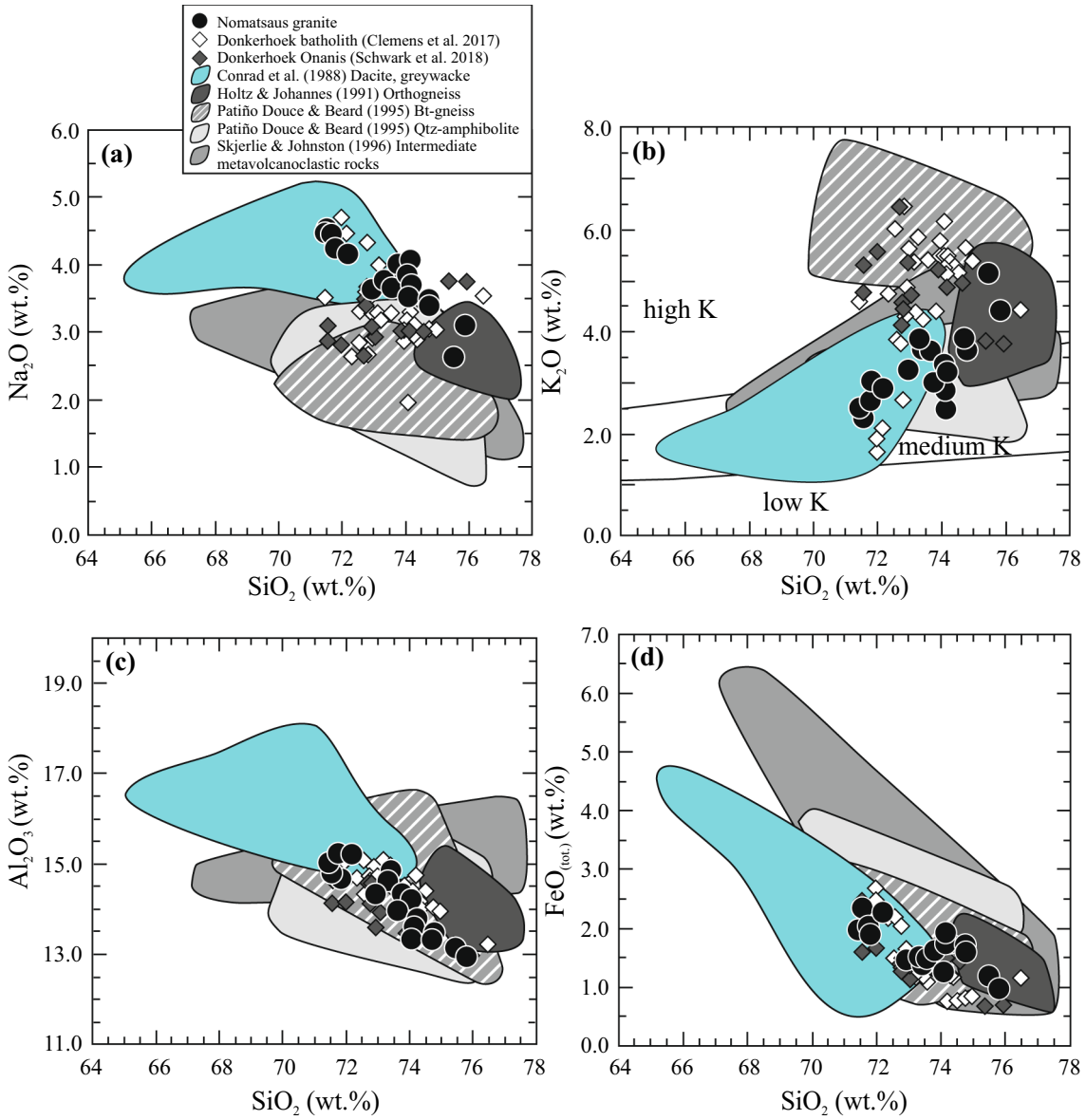

Fig. 14 Major element diagrams showing data of the Nomatsaus granite in comparison with experimental melts

isotopic composition of the Nomatsaus granite plots close to the upper crustal evolution curve of Zartman and Doe (1981) in the $^{207}Pb/^{204}Pb$ vs. $^{206}Pb/^{204}Pb$ and the $^{208}Pb/^{204}Pb$ vs. $^{206}Pb/^{204}Pb$ diagram (Fig. 10) and far from the fields of the lower crust-derived Achas, Bloedkoppie and Gawib plutons. The elevated $^{207}Pb/^{204}Pb$ ratios of the Nomatsaus granite imply that the granite is derived from the melting of upper crustal rocks containing an ancient Pb component, which is in line with the Proterozoic two-stage depleted-mantle Nd model ages that range from 1.3 to 1.5 Ga. Of particular importance is the occurrence of a metamorphosed dacite occurring ~40 km south of the Nomatsaus area on farm Terra Rossa. Virtually no data exist for the Terra Rossa dacite but Haack et al. (1982) reported Rb–Sr isotope data for this dacite that, when recalculated to 511 Ma, gives an $^{87}Sr/^{86}Sr$ initial ratio of ~0.7074 which is identical to the initial ratios obtained on the Nomatsaus samples.

In conclusion, the Donkerhoek batholith was sourced from meta-igneous (Schwark et al. 2018; this study) and metasedimentary rocks (Clemens et al. 2017). Minor additions came from the underlying southern basement through combined assimilation–fractional crystallization processes (this study).

Tectonic implications

The conditions necessary to generate the diverse igneous complexes in the Damara orogen are not clear and existing

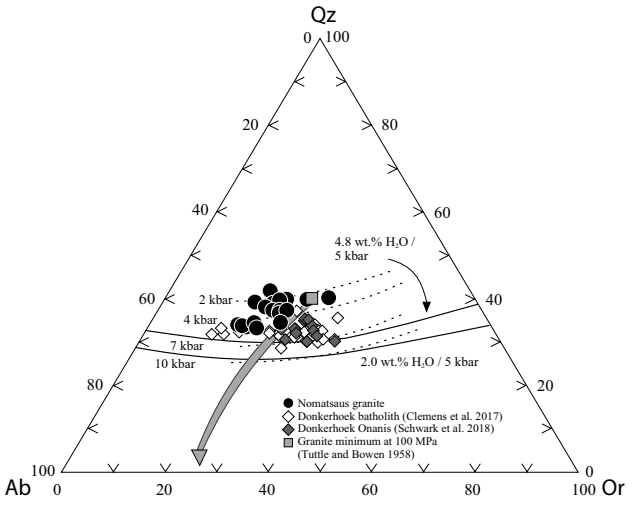

Fig. 15 Normative Qz–Ab–Or composition of the Nomatsaus granite relative to experimental H_2O-saturated minimum melt composition (dashed lines: Anderson and Bender 1989; solid lines: Long et al. 1986). Arrow denotes the evolution of granitic melts with the addition of phosphorous, fluorine and boron (Manning 1981; Pichavant 1987; London 1992a, b)

models range from classical subduction models (Barnes and Sawyer 1980) to ridge subduction and opening of an asthenospheric window (Meneghini et al. 2014), to intra-crustal heat production due to elevated K, Th and U contents (Haack et al. 1983; Jung et al. 2018; Longridge et al. 2017), and to intra-crustal heat transfer (Hartmann et al. 1983; Kröner 1982). Features that are considered to be essential in classical subduction zone settings are absent in the Damara orogen. High-P rocks (eclogites, blueschists) and early synorogenic igneous rocks with geochemical and isotopic features characteristic for mantle wedge- or slab-derived melts are unknown. In addition, the ratio of granite:granodiorite:diorite (96:2:2; Miller 2008) in the Damara orogen is atypical for the ratio among exposed igneous rocks in subduction-related continental margins (gabbro/diorite:tonalite/granodiorite:granite in proportions of 16:58:26; Pitcher 1978).

Age data for the Donkerhoek batholith range from ~ 540 to ~ 505 Ma (Blaxland et al. 1979; de Kock and Armstrong 2014; Clemens et al. 2017; Schwark et al. 2018, this study). According to Goscombe et al. (2017), this time span covers the period for collision, prograde burial and peak-metamorphism. The preservation of a typical Barrovian sequence in the Southern Zone (Fig. 1) implies common collision tectonics and the existence of a paired metamorphic belt consisting of medium pressure/medium temperature amphibolite-facies rocks on one side and low-pressure/high-temperature granulite-facies on the other side may indicate a subduction zone setting. This preservation would fit into the broader description given by Brown (2009a) where the term paired metamorphic belts …*may be used for penecontemporaneous belts of contrasting type of metamorphism that record different apparent thermal gradients, one warmer and the other colder, juxtaposed by plate tectonics processes…* (Brown 2009a). In addition, this may indeed apply to the Damara orogen where …*the suture and lower plate materials will register the imprint of low-to-intermediate dT/dP and the upper plate will register penecontemporaneous high dT/dP metamorphism commonly manifested at shallow crustal levels by the occurrence of granites in the rock record…* (Brown 2009b).

Although the orogen-wide N-MORB to E-MORB Matchless Amphibolite (Fig. 1) has been regarded as a remnant of oceanic crust, its thickness of a few hundred-meter maximum exposure questions its role in any subduction zone process because such unevolved, small-scale ridge segments are probably too buoyant to be subducted. This, and the lack of eclogites and blueschists, which are typical for the high-pressure rocks of paired metamorphic belts, together with a lack of calc-alkaline igneous rocks with unevolved isotope signatures raise the need for different explanations. Especially for the Donkerhoek batholith with its dominant crustal signature and the lack of appreciable amounts of mafic rocks, other models than common subduction zone models are needed. Therefore, alternative tectonic models for continent–continent collision settings with subduction and accretion of continental crust beneath the overriding plate (Moyen et al. 2017; Vanderhaeghe and Duchêne 2010) may be applied for the Damara orogen.

In general, coupling of the lithospheric mantle–crust system will facilitate the development of a subduction zone. Crust–mantle coupling also favors the generation of large amounts of mantle-derived igneous rocks owing to the water influx from the subducted plate (Moyen et al. 2017). Crustal melting is limited as the only extra heat is supplied by the magmas from the subduction process. Such a subduction scenario does not fit the observations from the Damara orogen. Although mafic rocks dominate the early igneous record of the Damara orogen, these rocks have a low volume and their isotope characteristics resemble evolved lower crustal rocks (Jung et al. 2002, 2015). Furthermore, the metamorphic environment seen in the overriding plate in the Damara orogen is low P/high T rather than high P/low T that is typical for common subduction zone environments. In contrast, decoupling of crust and mantle results in the accretion of crustal blocks and the most favorable process which generated crustal melts in the Damara orogen, as it will result in hot environments in the upper plate (Goscombe et al. 2017). Melting of the mantle due to limited influx of water is unlikely in this case. Such a hot environment seems to be essential for the generation of the Donkerhoek batholith, which is characterized by the dominance of crustal melts and the absence of mafic rocks. Age data indicate that the

generation of the batholith started at ~ 540 Ma. The onset of orogenic burial can be estimated to have started at ~ 575 Ma or somewhat earlier which is the age of the earliest mafic intrusions in the southern Central Zone (Milani et al. 2015). From ~ 575 to ~ 540 Ma, stacking of crustal domains with high K, Th, and U abundances increased the local radioactive heat production. This might represent the main heat source for the partial melting of metasedimentary, metaigneous and intercalated basement rocks at lower- to mid-crustal levels (Jung et al. 2018). Early models of anatexis in tectonically thickened crust using low heat production values (England and Thompson 1986; 0.–1.3 × 10^{-6} W/m^3) indicate that an increase of internal heat production by 50% raises peak temperatures by 150–200 °C at the bottom of the crust and thickening of the crust by a factor of 1.5–2 result in widespread anatexis at mid-crustal levels. Subsequent work (Chamberlain and Sonder 1990) indicated higher heat production values for crustal rocks (0.6–4.9 × 10^{-6} W/m^3) and calculations provided by Haack et al. (1983) showed even higher heat production values for the Damara orogen (2.5–8.8 × 10^{-6} W/m^3). For the Damara orogen, the thermal energy provided by the heat-producing elements after thickening was sufficient to cause the generation of granitic melts in the deeper crust. It is also predicted that melting events lag behind initiation of thrusting by several tens of millions of years (Zen 1987; Patiño Douce et al. 1990; Bea 2012). The amount of time depends on the thickness of depressed thrust sheets, the duration of the thickening event, the initial temperature and the amount of water present. Although these uncertainties cannot be resolved for the Damara orogen, the initiation of the magmatic event that caused the intrusion of the Donkerhoek batholith at ~ 540 Ma lag behind the onset of orogenic burial by at least ~ 35 Ma. Such a lag agrees well with the results of the one-dimensional model presented by Clark et al. (2011) who showed that with heat production values of 3.5–4.0 × 10^{-6} W/m^3 (which are well within the range of Damaran basement rocks and granites; Haack et al. 1983), temperatures of ~ 800 °C at the base of a 40 km-thick crust are achieved within 30–40 Ma. Similarly, Huerta et al. (1998) calculated that temperatures of 800 °C can be achieved in a 30 km-thick lithosphere using a heat production rate of ~ 4.0 × 10^{-6} W/m^3.

Summary and conclusion

This study illustrates that the ~ 511-Ma-old, late-tectonic Nomatsaus granite, as part of the Donkerhoek batholith, consists of peraluminous, medium- to high-K, calc-alkaline to calcic magnesian granites that intruded at mid-crustal levels. Negative correlations of Na_2O, $FeO_{(t.)}$, MgO, CaO, Al_2O_3, TiO_2, P_2O_5, Sr, Zr, Ga, U, and Th with respect to SiO_2 contents suggest fractionation of biotite, plagioclase, Fe-Ti oxides, zircon and monazite whereas a positive correlation of K_2O with increasing SiO_2 indicates accumulation of K-feldspar. Decreasing LREE and HREE abundances and rare-earth element modelling suggests that the most fractionated samples can be explained by fractionation of very small amounts of monazite and xenotime. Negative correlations between $f^{Sm/Nd}$ and initial εNd values, which are uncommon in granites, imply limited assimilation concomitant with fractionation of accessory phases. The $f^{Sm/Nd}$ vs. εNd correlation constrains the source of the Nomatsaus granite to εNd less than ~ − 3 and $f^{Sm/Nd}$ less than ~ 0.5. The moderately unradiogenic Sr (initial $^{87}Sr/^{86}Sr$: 0.7067–0.7082) and Nd (initial εNd: − 2.9 to − 4.8) isotope compositions of the Nomatsaus granites and the lack of correlation between previously published oxygen and $^{87}Sr/^{86}Sr$ isotope data (Haack et al. 1982) show that these features are inherited from the source. The Pb isotopic composition indicates that the Nomatsaus granite is derived from Mid-Proterozoic upper crustal rocks, which is compatible with two-stage DM Nd model ages of ~ 1.3 to ~ 1.5 Ga. Based on a comparison with experimental results, the most likely source for the Nomatsaus granite was a meta-dacite that melted at temperatures of 800–850 °C, pressures of 1.0 GPa (or less) and water-undersaturated conditions (x H_2O: 0.25–0.50). The application of monazite and zircon saturation thermometry using samples that lack potential monazite accumulation provided temperatures of 812 and 852 °C, respectively; similar to the experimental conditions. The Nomatsaus granite formed in a tectonic setting that is characterized by high crust-internal heat production, such as a continent–continent collisional setting involving decoupling between the mantle and the crust, which facilitates the production of granites with crustal signatures.

Appendix

Analytical techniques

Methods follow closely those described in Schwark et al. (2018). Whole rock powders were prepared using a jaw crusher and an agate mortar. Major and some trace elements were determined on fused lithium-tetraborate glass disks using a X-ray fluorescence spectrometer (XRF-Panalytical MagixPro) at Universität Hamburg using the software of Vogel and Kuipers (1987). Accuracy has been controlled by analyses of several international standards and the precision is 1–2% for major elements and 5–20% for trace elements depending on the concentration. Loss on ignition (LOI) was determined gravimetrically after heating the samples to 1050 °C for 3 h (Lechler and Desilets 1987). Samples with incomplete trace-element data (10 Rare-Earth Elements, REE) were determined using

ICP-AES techniques at Universität of Marburg following the procedure of Jung et al. (2003). Samples with a full set of trace elements, including 14 REE, were analyzed at Universität Kiel by ICP- MS following the procedures outlined in Garbe-Schönberg (1993). The precision is between 3 and 5% for trace elements relative to the recommended values of the international standard BIR-1, which was analyzed as an unknown together with the samples. For the Sr and Nd isotope analyses the samples were dissolved in concentrated HF-HNO_3 at 150 °C overnight using 7 ml Teflon vials. Subsequently, the samples were dried down and redissolved in 2.5 N HCl. Strontium and REE were separated using standard cation-exchange columns with a DOWEX AG 50 W-X 12 resin using 2.5 N HCl for Sr and 6 N HCl for the REE. Sr was purified on BIORAD© microcolumns filled with ca 50–100 µl TRISKEM© Sr-Resin (50–100 µm) operating with 6 M HNO_3 and 0.05 M HNO_3 eluents. Neodymium was separated from the other REE using 4 ml quarz glass columns filled with EICHROM© Ln Resin and 0.22 N HCl eluent. All isotope analyses were carried out at GEOMAR (Kiel) by thermal ionization mass spectrometry (TIMS) using a Thermo Scientific TRITON Plus for Sr, Nd and a Finigan MAT262 for Pb. Neodymium was run on Re double filaments and Sr was run on Re single filaments using a Ta_2O_5 emitter (Birck 1986). Neodymium isotopes were mass-bias corrected within run to $^{146}Nd/^{144}Nd = 0.7219$. Multiple measurements of LaJolla Nd along with the samples gave $^{143}Nd/^{144}Nd = 0.511844 \pm 0.000005$ (2SD; $n = 5$) in good agreement with the long-term reproducibility of 0.511843 ± 0.000006 (2SD; $n = 114$) over the period of the project (11/2014–09/2015). Sample data are reported relative to $^{143}Nd/^{144}Nd = 0.511850$ for La Jolla. Sr isotope ratios were mass-bias corrected within run to $^{86}Sr/^{88}Sr = 0.1194$. NBS987 measured along with the samples gave $^{87}Sr/^{86}Sr = 0.710243 \pm 0.000005$ (2SD, $n = 5$) in the first session and $^{87}Sr/^{86}Sr = 0.710253 \pm 0.000005$ in the second session. Sample data have been normalized to NBS987 $^{87}Sr/^{86}Sr = 0.710250$ for each session. For Pb isotope analyses, 10–15 mg of pure K-feldspar separates were washed with a mixture of 3:1 HCl/HNO_3 to remove surface contamination at 100 °C overnight and were subsequently rinsed three times with ultrapure water. After this treatment, the K-feldspar separates were leached three times in a mixture of concentrated HF/HNO_3, which resulted in a weight loss of ca. 50–70% and was then followed by digestion in concentrated HF and HNO_3. Samples were evaporated to dryness and converted to chloride, centrifuged and loaded on Teflon columns of DOWEX AG 1 × 8 anion exchange resin (100–200 mesh) in chloride form (Mattinson 1986). Matrix elements were eluted with 1 M HBr and not collected. The Pb fraction was eluted with 6 N HCl and cleaned in a second separation using the same columns. The Pb was loaded on Re single filaments following the H_3PO_4-silica gel method (Cameron et al. 1969). All measurements were corrected for mass fractionation by 0.11‰ per a.m.u. based on repeat measurements of NBS981 ($^{206}Pb/^{204}Pb = 16.902 \pm 0.010$, $^{207}Pb/^{204}Pb = 15.445 \pm 0.013$, $^{208}Pb/^{204}Pb = 36.553 \pm 0.041$; all errors 2SD, $n = 23$) and correction to NBS981 Pb double-spike corrected values ($^{206}Pb/^{204}Pb = 16.9427 \pm 0.0020$, $^{207}Pb/^{204}Pb = 15.5004 \pm 0.0021$, $^{208}Pb/^{204}Pb = 36.7277 \pm 0.0045$; all errors 2SD, $n = 19$) obtained on this instrument during the same period.

Acknowledgements Ulrike Westernströer and Dieter Garbe-Schönberg (U Kiel) are thanked for measurements of some samples by ICP-MS and Silke Hauff for help in the isotope laboratory at GEOMAR (Kiel). This study was funded through DFG grant Ju326/15 to SJ. Finally, we would like to thank Francois Moyen for recalculating our data for the triangular diagram presented in Moyen et al. (2017). This manuscript benefitted by comments from Enrique Merino Martínez and an unknown reviewer.

Funding Open Access funding enabled and organized by Projekt DEAL.

References

Anderson JL, Bender EE (1989) Nature and origin of Proterozoic A-type granitic magmatism in the southwestern United States of America. Lithos 23:19–52

Andrehs G, Heinrich W (1998) Experimental determination of REE distributions between monazite and xenotime: potential for temperature-calibrated geochronology. Chem Geol 149:83–96

Bacon CR, Druitt TH (1988) Compositional evolution of the zoned calcalkaline magma chamber of Mount Mazama, Crater Lake, Oregon. Contrib Miner Petrol 98:224–256

Barnes S-J, Sawyer EW (1980) An alternative model for the Damara Mobile Belt: ocean crust subduction and continental convergence. Precambr Res 13:297–336

Bea F (2012) The sources of energy for crustal melting and the geochemistry of heat-producing elements. Lithos 153:278–291

Bea F, Pereira MD, Stroh A (1994) Mineral/leucosome trace-element partitioning in a peraluminous migmatite (a laser-ablation-ICP-MS study). Chem Geol 117:291–312

Beard JS, Lofgren GE (1991) Dehydration melting and water-saturated melting of basaltic and andesitic greenstones and amphibolites at 1, 3 and 6.9 kb. J Petrol 32:365–401

Bergemann C, Jung S, Berndt J, Stracke A, Hauff F (2014) Generation of magnesian, high-K alkali-calcic granites and granodiorites from amphibolitic continental crust in the Damara orogen, Namibia. Lithos 198–199:217–233

Birck JL (1986) Precision K–Rb–Sr isotopic analysis: application to Rb–Sr chronology. Chem Geol 56(1):73–83

Blaxland A, Gohn E, Haack U, Hoffer E (1979) Rb/Sr ages of late-tectonic granites in the Damara Orogen, Southwest Africa/Namibia. Neues Jb Mineral Monat 11:498–508

Boynton WV (1984) Geochemistry of rear earth elements: meteorite studies. In: Henderson P (ed) Rare Earth element geochemistry. Elsevier, New York, pp 63–114

Brown M (2009a) Metamorphic patterns in orogenic systems and the geological record. In: Cawood PA, Kröner A (eds) Accretionary orogens in space and time. Special publications, vol 318. Geological Society, London, pp 37–74

Brown M (2009) Paired metamorphic belts revisited. Gondwana Res 18:46–59

Cameron AE, Smith DH, Walker RL (1969) Mass spectrometry of nanogram-size samples of lead. Anal Chem 41:525–526

Castro A (2013) Tonalite-granodiorite suites as cotectic systems: a review of experimental studies with applications to granitoids petrogenesis. Earth Sci Rev 124:68–95

Chamberlain CP, Sonder LJ (1990) Heat-producing elements and the thermal and baric patterns of metamorphic belts. Science 250:763–769

Chappell BW (1999) Aluminium saturation in I- and S-type granites and the characterization of fractionated haplogranites. Lithos 46:535–551

Chappell BW, Stephens WE (1988) Origin of infracrustal (I-type) granite magmas. Trans R Soc Edinb Earth Sci 79:71–86

Chappell BW, White AJR (2001) Two contrasting granite types: 25 years later. Aust J Earth Sci 48:489–499

Chappell BW, Bryant CJ, Wyborne D (2012) Peraluminous I-type granites. Lithos 153:142–153

Clark C, Fitzsimons ICW, Healy D, Harley SL (2011) How does the continental crust get really hot? Elements 7:235–240

Clemens JD (2018) Granitic magmas with I-type affinities, from mainly metasedimentary sources: the Harcourt batholith of southeastern Australia. Contrib Miner Petrol 173:93

Clemens JD, Stevens G, Farina F (2011) The enigmatic source of I-type granites: the peritectic connexion. Lithos 126:174–181

Clemens JD, Buick IS, Kisters AFM, Frei D (2017) Petrogenesis of the granitic Donkerhuk batholith in the Damara belt of Namibia: protracted, syntectonic, short-range, crustal magma transfer. Contrib Miner Petrol 172:50

Coleman DS, Glazner AF (1997) The Sierra Crest magmatic event: rapid formation of juvenile crust during the late Cretaceous in California. Int Geol Rev 39:768–787

Collins WJ, Beams SD, White AJR, Chappell BW (1982) Nature and origin of A-type granites with particular reference to southeastern Australia. Contrib Miner Petrol 80:189–200

Conrad WK, Nicholls IA, Wall VJ (1988) Water-saturated and -undersaturated melting of metaluminous and peraluminous crustal compositions at 10 kb: evidence for the origin of silicic magmas in the Taupo volcanic zone, New Zealand, and other occurrences. J Petrol 29:765–803

Copeland P, Parrish RR, Harrison TM (1988) Identification of inherited radiogenic Pb in monazite and implications for U–Pb systematics. Nature 333:760–763

Cross CB, Diener JFA, Fagereng Å (2015) Metamorphic imprint of accretion and ridge subduction in the Pan-African Damara Belt, Namibia. J Metamorph Geol 33:633–648

de Kock GS, Armstrong R (2014) SHRIMP dating on magmatic rocks from the Karibib–Otjimbingwe region, Namibia. In: Roy Miller Symposium, The Geological Society of Namibia, Windhoek, Namibia, p 41

DePaolo DJ (1981) Trace element and isotopic effects of combined wall rock assimilation and fractional crystallization. Earth Planet Sci Lett 53:189–202

England PC, Thompson AB (1986) Some thermal and tectonic models for crustal melting in continental collision zones. In: Coward MP, Ries A (eds) Collision tectonics, vol 19. Geological Society Special Publication, pp 83–94

Frost CD, Frost BR (1997) Reduced rapakivi-type granites: the tholeiite connection. Geology 25:647–650

Frost BR, Barnes CG, Collins WJ, Arculus RJ, Ellis DJ, Frost CD (2001) A geochemical classification for granitic rocks. J Petrol 42:2033–2048

Gao P, Zheng Y-F, Zhao Z-F (2016) Experimental melts from crustal rocks: a lithochemical constraint on granite petrogenesis. Lithos 266–267:133–157

Garbe-Schönberg C-D (1993) Simultaneous determination of thirty-seven trace elements in twenty-eight international rock standards by ICP-MS. Geostand Newsl 17:81–97

Glazner AF, Bartley JM, Coleman DS, Gray W, Taylor RZ (2004) Are plutons assembled over millions of years by amalgamation from small magma chambers? GSA Today 14:4–11

Goscombe B, Foster DA, Gray D, Wade B (2017) Metamorphic response and crustal architecture in a classic collisional orogen: the Damara Belt, Namibia. Gondwana Res 52:80–124

Haack U, Hoefs J, Gohn E (1982) Constraints on the origin of Damaran granites by Rb/Sr and $\delta^{18}O$ data. Contrib Miner Petrol 79:279–289

Haack U, Gohn E, Hartmann O (1983) Radiogenic heat generation in Damaran rocks. In: Miller RMG (ed) Evolution of the Damara Orogen of South West Africa/Namibia, vol 11. Geological Society of South Africa, Special Publication, pp 225–232

Hall D, Kisters A (2016) Episodic granite accumulation and extraction from the mid-crust. J Metamorph Geol 34:483–500

Harrison TM, Watson EB (1984) The behavior of apatite during crustal anatexis: equilibrium and kinetic considerations. Geochim Cosmochem Acta 48:1467–1477

Hartmann O, Hoffer E, Haack U (1983) Regional metamorphism in the Damara Orogen: interaction of crustal motion and heat transfer. In: Miller RMG (ed) Evolution of the Damara Orogen of South West Africa/Namibia, vol 11. Geological Society of South Africa, Special Publication, pp 233–241

Hawkesworth CJ, Kramers JD, Miller RMcG, (1981) Old model Nd ages in Namibian Pan-African rocks. Nature 289:278–282

Holtz F, Johannes W (1991) Genesis of peraluminous granites I. Experimental investigation of melt compositions at 3 and 5 kb and various H_2O activities. J Petrol 32:935–958

Hu J-Q, Li X-W, Xu J-F, Mo X-X, Wang F-Y, Yu H-X, Shan W, Xing H-Q, Huang X-F, Dong G-C (2019) Generation of coeval metaluminous and muscovite-bearing peraluminous granitoids in the same composite pluton in West Qinling, NE Tibetan Plateau. Lithos 344–345:374–392

Huerta AD, Royden LH, Hodges KV (1998) The thermal structure of collisional orogens as a response to accretion, erosion, and radiogenic heat production. J Geophys Res 103:15287–15302

Jacobsen SB, Wasserburg GJ (1980) Sm–Nd isotopic evolution of chondrites. Earth Planet Sci Lett 50:139–155

Jung S, Hauff F (2021) Petrogenesis of a low-$^{87}Sr/^{86}Sr$, two-mica, garnet-bearing leucogranite (Donkerhoek batholith, Damara orogen, Namibia). J Afr Earth Sci 174:104055

Jung S, Mezger K, Hoernes S (1998) Petrology and geochemistry of syn- to post-collisional metaluminous A-type granites—a major and trace element and Nd–Sr–Pb–O isotope study from the Proterozoic Damara Belt, Namibia. Lithos 45:147–175

Jung S, Hoernes S, Masberg P, Hoffer E (1999) The petrogenesis of some migmatites and granites (Central Damara orogen, Namibia): evidence for disequilibrium melting, wall-rock contamination and crystal fractionation. J Petrol 40:1241–1269

Jung S, Hoernes S, Mezger K (2000) Geochronology and petrology of migmatites from the Proterozoic Damara Belt—importance of

episodic fluid-present disequilibrium melting and consequences for granite petrology. Lithos 51(3):153–179
Jung S, Hoernes S, Mezger K (2002) Synorogenic melting of mafic lower crust: constraints from geochronology, petrology and Sr, Nd, Pb and O isotope geochemistry of quartz diorites (Damara orogen, Namibia). Contrib Miner Petrol 143:551–566
Jung S, Mezger K, Hoernes S (2003) Petrology of basement-dominated terranes: II. Contrasting isotopic (Sr, Nd, Pb and O) signatures of basement-derived granites and constraints on the source region of granite (Damara orogen, Namibia). Chem Geol 199:1–28
Jung S, Mezger K, Nebel O, Kooijman E, Berndt J, Hauff F, Müncker C (2011) Origin of meso-Proterozoic post-collisional leucogranite suites (Kaokoveld, Namibia): constraints from geochronology and Nd, Sr, Hf and Pb isotopes. Contrib Miner Petrol 163:1–17
Jung S, Kröner A, Hauff F, Masberg P (2015) Petrogenesis of syn-orogenic diorite-granodiorite-granite complexes in the Damara Belt, Namibia: constraints from U–Pb zircon ages and Sr–Nd–Pb isotopes. J Afr Earth Sci 101:253–265
Jung S, Brandt S, Bast R, Scherer EE, Berndt J (2018) Metamorphic petrology of a high-T/low-P granulite terrane (Damara belt, Namibia)—constraints from pseudosection modelling and high-precision Lu–Hf garnet-whole rock dating. J Metamorph Geol 37:41–69
Kasch KW (1983) Continental collision, suture propagation and thermal relaxation: a plate tectonic model for the Damara orogen in central Namibia. In: Miller RMG (ed) Evolution of the Damara Orogen of South West Africa/Namibia, vol 11. Geological Society of South Africa, Special Publication, pp 423–429
Kröner A (1982) Rb–Sr geochronology and tectonic evolution of the Pan-African Damara belt of Namibia, southwestern Africa. Am J Sci 282:1471–1507
Kruger T, Kisters A (2016) Magma accumulation and segregation during regional-scale folding: the Holland's Dome granite injection complex, Damara belt, Namibia. J Struct Geol 89:1–18
Le Breton N, Thompson AB (1988) Fluid-absent (dehydration) melting of biotite in metapelites in the early stages of crustal anataxis. Contrib Miner Petrol 99:226–237
Lechler PJ, Desilets MO (1987) A review of the use of loss on ignition as a measurement of total volatiles in whole-rock analysis. Chem Geol 63:341–344
Liew TC, McCulloch MT (1985) Genesis of granitoid batholiths of Peninsular Malaysia and implications for models of crustal evolution—evidence from a Nd–Sr isotopic and U–Pb zircon study. Geochim Cosmochim Acta 49:587–600
Loiselle MC, Wones DR (1979) Characteristics and origin of anorogenic granites. Geol Soc Am Abst Prog 11:468
London D (1992) Phosphorus in S-type magmas: the P_2O_5 content of feldspars from peraluminous granites, pegmatites, and rhyolites. Am Miner 77:126–145
London D (1992) The application of experimental petrology to the genesis and crystallization of granitic pegmatites. Can Mineral 30:499–540
Long LE, Sial AN, Nekvasil H, Borba GS (1986) Origin of granite at Cabo de Santo Agostinho, Northeast Brazil. Contrib Miner Petrol 92:341–350
Longridge L, Gibson RL, Kinnaird JA, Armstrong RA (2017) New constraints on the age and conditions of LPHT metamorphism in the southwestern Central Zone of the Damara Belt, Namibia and implications for tectonic setting. Lithos 281:361–382
Manning DAC (1981) The effect of fluorine on liquidus phase relationships in the system Qz-Ab-Or with excess water at 1 kb. Contrib Mineral Petrol 76(2):206–215
Masberg HP, Hoffer E, Hoernes S (1992) Microfabrics indicating granulite-facies metamorphism in the low-pressure central Damara Orogen, Namibia. Precambr Res 55:243–257
Mattinson JM (1986) Geochronology of high pressure-low temperature Franciscan metabasites: a new approach using the U–Pb system. Geol Soc Am Mem 164:95–105
McDermott F, Harris NBW, Hawkesworth CJ (1996) Geochemical constraints on crustal anataxis: a case study from the Pan-African Damara granitoids of Namibia. Contrib Miner Petrol 123:406–423
McDermott F, Harris NBW, Hawkesworth CJ (2000) Geochemical constraints on the petrogenesis of Pan-African A-type granites in the Damara Belt, Namibia. Commun Geol Surv Namib 12:157–167
Meneghini F, Kisters A, Buick I, Fagereng A (2014) Fingerprints of late Neoproterozoic ridge subduction in the Pan-African Damara belt, Namibia. Geology 42:903–906
Merino Martínez E, Villaseca C, Orejana D, Pérez-Soba C, Belousova E, Andersen T (2014) Tracing magma sources of three different S-type peraluminous granitoid series by in situ U–Pb geochronology and Hf-isotope zircon composition: the Variscan Montes de Toledo batholith (central Spain). Lithos 200–201:273–298
Michard A, Gurriet P, Soudant M, Albarède F (1985) Nd isotopes in French Phanerozoic shales: external vs. internal aspects of crustal evolution. Geochim Cosmochim Acta 49:601–610
Middlemost EAK (1994) Naming materials in the magma/igneous rock system. Earth Sci Rev 37:215–224
Milani L, Kinnaird JA, Lehmann J, Naydenov KV, Saalmann K, Frei D, Gerdes A (2015) Role of crustal contribution in the early stage of the Damara Orogen, Namibia: new constraints from combined U–Pb and Lu–Hf isotopes from the Goas Magmatic Complex. Gondwana Res 28:961–986
Miller CF (1985) Are strongly peraluminous magmas derived from pelitic sedimentary sources? J Geol 93:673–689
Miller RMG (2008) The geology of Namibia. Neoproterozoic to Lower Phanerozoic. Ministry of Mines and Energy, vol 2 Geological Survey. Windhoek
Montel JM (1993) A model for monazite/melt equilibrium and application to the generation of granitic magmas. Chem Geol 110:127–146
Moyen J-F, Laurent O, Chelle-Michou C, Couzinié S, Vanderhaeghe O, Zeh A, Villaros A, Gardien V (2017) Collision vs. subduction-related magmatism: two contrasting ways of granite formation and implications for crustal growth. Lithos 277:154–177
Ohta T, Arai H (2007) Statistical empirical index of chemical weathering in igneous rocks: a new tool for evaluating the degree of weathering. Chem Geol 240:280–297
Ostendorf J, Jung S, Berndt-Gerdes J, Hauff F (2014) Syn-orogenic high-temperature crustal melting: geochronological and Nd–Sr–Pb isotope constraints from basement-derived granites (Central Damara Orogen, Namibia). Lithos 192–195:21–38
Osterhus L, Jung S, Berndt J, Hauff F (2014) Geochronology, geochemistry and Nd, Sr and Pb isotopes of syn-orogenic granodiorites and granites (Damara orogen, Namibia)—arc-related plutonism or melting of mafic crustal sources? Lithos 200–201:386–401
Patiño Douce AE, Beard JS (1995) Dehydration-melting of biotite gneiss and quartz amphibolite from 3 to 15 kbar. J Petrol 36:707–738
Patiño Douce AE, Humphries DE, Johnston AD (1990) Anatexis and metamorphism in tectonically thickened crust exemplified by the Sevier Hinterland, Western North America. Earth Planet Sci Lett 97:290–315
Paul A, Jung S, Romer RL, Stracke A, Hauff F (2014) Petrogenesis of synorogenic high-temperature leucogranites (Damara orogen, Namibia): constraints from U–Pb monazite ages and Nd, Sr and Pb isotopes. Gondwana Res 25:1614–1626
Pichavant M (1987) An experimental study of the effect of boron on a water saturated haplogranite at 1 kbar vapour pressure. Geological applications. Contrib Miner Petrol 76:430–439

Pitcher WS (1978) Anatomy of a batholith. J Geol Soc Lond 135:157–182

Prave AR (1996) Tale of three cratons: tectonostratigraphic anatomy of the Damara orogen in northwestern Namibia and the assembly of Gondwana. Geology 24:1115–1118

Rapp RP, Watson EB (1986) Monazite solubility and dissolution kinetics: implications for the thorium and light rare earth chemistry of felsic magmas. Contrib Miner Petrol 94:304–316

Rapp RP, Ryerson FJ, Miller CF (1987) Experimental evidence bearing on the stability of monazite during crustal anatexis. Geophys Res Lett 14:307–310

Sawka WN, Banfield JF, Chappell BW (1986) A weathering-related origin of widespread monazite in S-type granites. Geochim Cosmochim Acta 50:171–175

Schwark L, Jung S, Hauff F, Garbe-Schönberg D, Berndt J (2018) Generation of syntectonic calc-alkaline, magnesian granites through remelting of pre-tectonic igneous sources—U–Pb zircon ages and Sr, Nd and Pb isotope data from the Donkerhoek granite (southern Damara orogen, Namibia). Lithos 310–311:314–331

Seth B, Jung S, Hoernes S (2002) Isotope constraints on the origin of Pan-African granitoids rocks in the Kaoko belt, NW Namibia. S Afr J Geol 105:179–192

Shirey SB, Hanson GN (1986) Mantle heterogeneity and crustal recycling in Archean granite greenstone belts: evidence from Nd isotopes and trace elements in the Rainy Lake area, Superior Province, Ontario, Canada. Geochim Cosmochim Acta 50:2631–2651

Simon I, Jung S, Romer RL, Garbe-Schönberg D, Berndt J (2017) Geochemical and Nd–Sr–Pb isotope characteristics of synorogenic lower crust-derived granitoids (Central Damara orogen, Namibia). Lithos 274–275:397–411

Skjerlie KP, Johnston AD (1996) Vapour-absent melting from 10 to 20 kbar of crustal rocks that contain multiple hydrous phases: implications for anataxis in the deep to very deep continental crust and active continental margins. J Petrol 37:661–691

Stammeier J, Jung S, Romer RL, Berndt J, Garbe-Schönberg D (2015) Petrology of ferroan alkali-calcic granites: synorogenic high-temperature melting of underplated felsic lower crust (Damara orogen, Namibia). Lithos 224–225:114–125

Stepanov AS, Hermann J, Rubatto D, Rapp RP (2012) Experimental study of monazite/melt partitioning with implications for the REE, Th and U geochemistry of crustal rocks. Chem Geol 300–301:200–220

Turner SP, Foden JD, Morrison RS (1992) Derivation of some A-type magmas by fractionation of basaltic magma: an example from the Padthaway Ridge, South Australia. Lithos 28:151–179

Vanderhaeghe O, Duchêne S (2010) Crustal-scale mass transfer, geotherm and topography at convergent plate boundaries. Terra Nova 22:315–323

Vielzeuf D, Holloway JR (1988) Experimental determination of the fluid-absent melting relations in the pelitic system. Contrib Miner Petrol 98:257–276

Villa IM, De Bièvre P, Holden NE, Renne PR (2015) IUPAC_IUGS recommendation on the half-life of ^{87}Rb. Geochim Cosmochim Acta 172:387–392

Vogel W, Kuipers G (1987) A pre-calibrated program for geological applications, Phillips New Developments. X-Ray Spectrom 11:2–8

Watson EB, Green TH (1981) Apatite/liquid partition coefficients for the rare earth elements and strontium. Earth Planet Sci Lett 56:405–421

Watson EB, Harrison TM (1983) Zircon saturation revisited: temperature and composition effects in a variety of crustal magma types. Earth Planet Sci Lett 64:295–304

Wenner JM, Coleman DS (2004) Magma mixing and cretaceous crustal growth: geology and geochemistry of granites in the Central Sierra Nevada batholith, California. Int Geol Rev 46:880–903

Wolf M, Romer RL, Glodny J (2019) Isotope disequilibrium during partial melting of metasedimentary rocks. Geochim Cosmochim Acta 257:163–183

Yakymchuk C, Brown M (2014) Behaviour of zircon and monazite during melting. J Geol Soc Lond 171:465–479

Zartman RE, Doe BR (1981) Plumbotectonics—the model. Tectonophysics 75:135–162

Zen E.-an. (1987) Thermal modeling by stepwise anatexis in a thrust-thickened sialic crust. Trans R Soc Edinb Earth Sci 79:223–235

Ziegler U, Stoessel G (1993) Age determinations in the Rehoboth Basement Inlier, Namibia, vol 14. Geological Survey of Namibia, Ministry of Mines and Energy, Memoir, pp 1–106